

# PCCP

Accepted Manuscript



This is an *Accepted Manuscript*, which has been through the Royal Society of Chemistry peer review process and has been accepted for publication.

*Accepted Manuscripts* are published online shortly after acceptance, before technical editing, formatting and proof reading. Using this free service, authors can make their results available to the community, in citable form, before we publish the edited article. We will replace this *Accepted Manuscript* with the edited and formatted *Advance Article* as soon as it is available.

You can find more information about *Accepted Manuscripts* in the [Information for Authors](#).

Please note that technical editing may introduce minor changes to the text and/or graphics, which may alter content. The journal's standard [Terms & Conditions](#) and the [Ethical guidelines](#) still apply. In no event shall the Royal Society of Chemistry be held responsible for any errors or omissions in this *Accepted Manuscript* or any consequences arising from the use of any information it contains.

# Resolving stress tensor components in space from polarized Raman spectra: polycrystalline alumina

Giuseppe Pezzotti<sup>a,\*</sup> and Wenliang Zhu<sup>a</sup>

A method of Raman spectroscopic analysis has been proposed for evaluating tensorial stress fields stored in alumina polycrystals with a corundum structure ( $\alpha$ -Al<sub>2</sub>O<sub>3</sub>). Raman selection rules for all the vibrational modes of the structure were expanded into explicit functions of both 3 Euler angles in space and 4 Raman tensor elements (RTE) of corundum. A theoretical treatment has then been worked out according to the phonon deformation potential (PDP) formalism, which explicitly expressed the changes in force constants under stress in matrixial form. Close-form solutions could be obtained for the matrix eigenvalues as a function of 9 unknown variables, namely 6 independent stress tensor components and 3 Euler angles in space, the latter parameters being representatives of local crystal orientation. Successively, two separate sets of Raman calibration experiments were performed for the determination of both RTE and PDP constants of the corundum structure of alumina. Calibration experiments provided a quantitative frame to the newly developed Raman formalism. Polarized Raman spectra were systematically recorded in both single-crystalline and polycrystalline samples, with both  $A_{1g}$  and  $E_g$  vibrational bands being characterized. Regarding polycrystalline samples, a validation of the proposed Raman method could be given through a comparison between Raman and fluorescence data collected at the same locations across an alumina/metal interface embedded in a steeply graded residual stress field.

## 1 Introduction

Microscopic stress analyses in  $\alpha$ -Al<sub>2</sub>O<sub>3</sub> samples have so far predominantly been performed by exploiting the stress sensitivity of the ruby doublet of fluorescence emitted from chromophoric (Cr<sup>3+</sup>) isovalent impurities (i.e., natively solved into the corundum lattice at substitutional sites for Al<sup>3+</sup>).<sup>1-4</sup> Stress assessments by fluorescence spectroscopy rely on a straightforward formalism (often referred to as the piezospectroscopic approach) that expresses the spectral shifts of the ruby lines as the scalar product of two second-rank tensors, namely the stress tensor and the tensor of the so-called piezo-spectroscopic constants of the crystal. The structure of this latter tensor has been regarded as a crystal property, with the tensor being purely diagonal in the reference frame of the principal axes of the crystal.<sup>5</sup> The diagonal components of the piezo-spectroscopic tensor of the chromophoric lines of sapphire, as well as the cumulative piezospectroscopic coefficient measured in response to an applied hydrostatic stress, have long and extensively been characterized in the literature.<sup>6-8</sup> Attempts have also been made in separating the hydrostatic and the deviatoric components of the stress tensor according to a (slightly) different response to stress of the two chromophoric lines.<sup>9,10</sup> However, the approach to stress analysis using the chromophoric emission of alumina ceramics, despite being based on a simple principle and having proved successful in several technological purposes, leaves unsolved basic issues related to the resolution of individual stress tensor components.

Sapphire and polycrystalline Al<sub>2</sub>O<sub>3</sub> possess relatively sharp Raman bands, which also exhibit a dependence on stress of

their spectroscopic shifts.<sup>11-13</sup> Investigations of the stress dependence of the Raman spectrum of  $\alpha$ -Al<sub>2</sub>O<sub>3</sub>, however, have proved less popular through the years than those based on fluorescence assessments, both in scientific studies and technological applications. Several reasons could have contributed to such a lack of experimental accessibility to the Raman method. The main reasons, which are also common shortcomings in general Raman spectroscopic measurements, could be listed as follows: (i) the Raman spectrum of corundum Al<sub>2</sub>O<sub>3</sub> is generally weaker than the ruby fluorescence doublet, which involves longer acquisition times and, possibly, larger errors in the fitting procedure to locate the band maximum; (ii) the stress dependence of Raman bands, unlike the case of fluorescence bands, is quite sensitive to the local crystallographic orientation at the measurement site; and, thus, necessarily requires quantitative notions of crystal axes in 3 local Euler angles. Such dependence should rigorously be embedded in the algorithm for a correct stress assessment; and, (iii) the phenomenological equations that represent the stress dependence of the chromophoric lines, are based on a simple formalism whose output is a scalar quantity that represents the trace of the stress tensor (namely, the algebraic sum of the diagonalized components of the principal stress tensor). On the other hand, the set of equations of the PDP formalism, which is needed for stress analysis by Raman, is more complex because it links the shift of each Raman band observed in the spectrum to all the individual stress tensor components stored in the crystal structure. Besides such inherent complexity, additional complications might arise due to a loss of degeneracy (i.e., in degenerate Raman modes) in the presence of stress. In substance, Raman-based algorithms potentially lead to detailed

information on the stress state of the crystal lattice, but also prove comparatively more complex and cumbersome than their correspondent ones in fluorescence analyses.

The convoluted physical circumstances that give rise to the above points (ii) and (iii) might indeed have represented common issues in discouraging researchers to use the Raman method in stress analysis, especially when dealing with non-cubic crystals. Note that the PDP formalisms, which directly link strain (rather than stress) to the spectral shift of vibrational bands,<sup>14</sup> have already been applied to several types of single-crystalline structure. Such studies mainly include cubic crystals, such as silicon,<sup>15</sup> germanium and zinc-blend-type semiconductors.<sup>16</sup> However, also less symmetric crystal structures, although less frequently, have been approached through systematic PDP studies; namely, the trigonal structure of  $\alpha$ -quartz,<sup>17</sup> and the wurtzitic structures of gallium nitride<sup>18</sup> and cadmium sulfide<sup>19</sup>. Our research group has recently reported on calibrations of RTE and PDP constants for tetragonal single-crystalline and textured polycrystalline barium titanate,<sup>20,21</sup> for the trigonal structure of lithium niobate single-crystals,<sup>20,22</sup> for the wurtzitic structure of aluminium nitride,<sup>23</sup> and for the corundum structure of sapphire.<sup>24,25</sup> However, quantitative applications of PDP algorithms to polycrystalline samples yet remain conspicuously missing in the available literature.

In this paper, we attempt to extend our previous RTE and PDP studies on sapphire to a quantitative stress analysis of polycrystalline  $\text{Al}_2\text{O}_3$ . The proposed procedure and the newly developed algorithms enable us to decode, through concurrently monitoring the shifts of 6 polarized Raman bands, quantitative information of local crystallographic orientation and the full set of stress tensor components. The validity of this procedure is then checked by comparing the results of stress analyses by Raman with those more conventional and better established by fluorescence piezo-spectroscopy. Analyses by these two different methods are performed at exactly the same locations in a highly graded stress field associated to an  $\text{Al}_2\text{O}_3$ /metal bonded interface. As previously mentioned, the main driving force for this study has been the quite unique possibility of exploiting a tensorial stress deconvolution from the different behaviors of selected Raman bands, which otherwise results hardly accessible through fluorescence piezo-spectroscopic procedures. However, an additional driving force in developing PDP algorithms for polycrystalline samples has been the possibility to exploit the smaller size of the Raman probe as compared to the fluorescence one, thus obtaining a better spatial resolution.<sup>26-28</sup> High spatial resolution indeed represents a desirable characteristic in correctly assessing steeply graded residual stress fields as those usually developed in polycrystalline samples, especially in non-cubic structures.<sup>29</sup> For the same laser excitation source, a fairly large difference in probe size between Raman and fluorescence emissions in  $\text{Al}_2\text{O}_3$  ceramics can be found, which mainly arises from broadening of the latter probe. Broadening of the fluorescence probe originates from a peculiar phenomenon of absorption and re-emission of ruby line photons at  $\text{Cr}^{3+}$  sites.<sup>30</sup> Such phenomenon does not occur in the spectral region of Raman emission in alumina.

## 2 Theoretical background

### 2.1 Selection rules and Raman tensor elements in corundum $\text{Al}_2\text{O}_3$ .

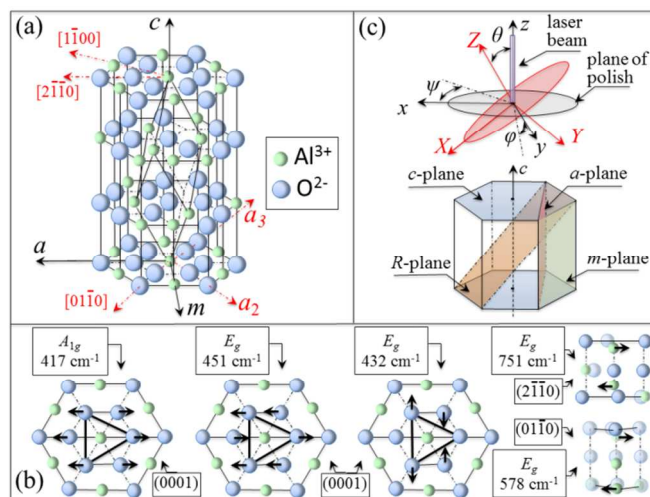


**Fig. 1:** Schematic draft of the corundum structure of  $\alpha\text{-Al}_2\text{O}_3$  (a), and of its main vibrational modes (b). In (c), drafts are shown of the principal planes of investigation within the corundum crystal structure and our choice of Cartesian and Euler angles in three dimensions.

The crystal structure of aluminium oxide, also referred to as the corundum structure, belongs to the ditrigonal-scalenohedral class of the trigonal symmetry  $D_{3d}^6$  ( $R\bar{3}C$ ) (Fig. 1(a)). The crystal lattice of  $\alpha\text{-Al}_2\text{O}_3$ , consisting of  $\text{Al}^{3+}$  and  $\text{O}^{2-}$  ions, takes the form of the closest hexagonal packing. The cations, displaced into a crystalline field at the octahedral hollows between the closely packed oxygen anions, fill two thirds of the hollows. The spatial arrangement of the anions is referred to as the “corundum motive”, according to which the interchanging octahedron positions of the cations are replicated within the structure by every three layers. The arrangement of the structural units along the third-order axis is then replicated in stacking of six anionic layers and six intermediate cationic layers. In the crystal lattice of single-crystal sapphire, two structurally elementary cells, namely the hexagonal and the rhombohedral, can be located. The irreducible representation for the optical modes of the  $\text{Al}_2\text{O}_3$  corundum crystal is:<sup>31-33</sup>

$$\Gamma = 2A_{1g} + 2A_{1u} + 3A_{2g} + 3A_{2u} + 5E_g + 5E_u \quad (1)$$

where  $A_{1g}$  contains two and  $E_g$  five Raman active modes (Fig. 1(b)), and the  $A_{2u}$  and  $E_u$  modes are either infrared active or acoustic modes. Note that the  $E_u$  modes may split into a longitudinal and a transverse representation because of the macroscopic field associated with the longitudinal polar modes. Moreover, since the unit cell has a centre of symmetry, in first approximation, all vibrations that are Raman allowed should be infrared forbidden and vice versa. More specifically, lattice vibrations with symmetry  $A_{1g}$  and  $E_g$  are Raman active and infrared inactive, while the  $A_{2u}$  and  $E_u$  vibrations are inactive in both infrared and Raman experiments. The basis functions for the representations of the  $A_{1g}$  and  $E_g$  modes of the  $D_{3d}$  point group are listed in Table 1.

**Table 1** Basis functions appropriate for the representations of the  $A_{1g}$  and  $E_g$  modes of the  $D_{3d}$  point group.

$D_{3d}$	$E$	$2C_3$	$3C_2$	$i$	$2S_3$	$3\sigma_d$	Basis functions
$A_{1g}$	1	1	1	1	1	1	$X^2 + Y^2, Z^2$
$E_g$	2	-1	0	2	-1	0	$(XZ, YZ); (X^2 - Y^2, XY); (R_x, R_y)$

Figure 2 shows the Raman spectrum of single-crystal sapphire as collected on different crystallographic planes and according to different polarization configurations. In inset, labels show the assignment of the Raman bands.<sup>34,35</sup> In total, we could resolve 7 different bands. In the recorded spectra, the bands located at around 417 and 645  $\text{cm}^{-1}$  belonged to the  $A_{1g}$  vibrational mode. On the other hand, bands located at around 378, 430, 451, 578, and 750  $\text{cm}^{-1}$  were assigned to the  $E_g$  mode. Depending on the crystallographic plane studied, some vibrational band resulted maximized or annihilated in its intensity (e.g., the  $E_g$  band located at around 750  $\text{cm}^{-1}$ , which results maximized on the  $c$ -plane and annihilated on the  $a$ -plane of sapphire). This is a direct consequence of the Raman selection rules discussed hereafter. However, it is important to note here the availability of more than six independent bands, which is a fundamental prerequisite for tensor-resolved stress analyses, as shown in a later section.

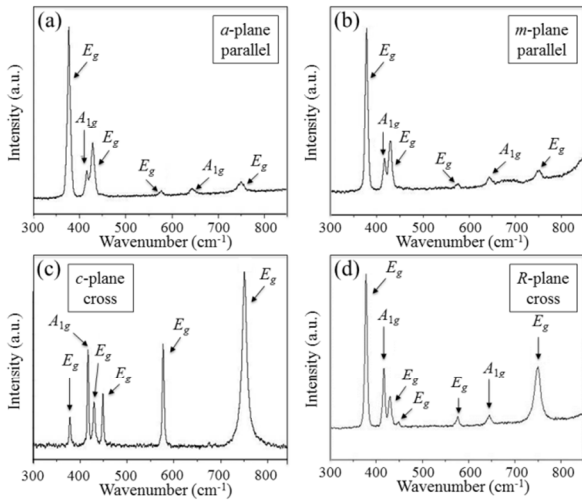


**Fig. 2:** Raman spectra of sapphire single-crystal as detected with the polarized laser beam focused on the  $a$ -plane (parallel probe configuration) (a), the  $m$ -plane (parallel probe configuration) (b), the  $c$ -plane (cross probe configuration) (c), and the  $R$ -plane (cross probe configuration) (d).

The scattered Raman intensity,  $I_i$ , of the optical mode in the case of a back-scattering configuration can generally be represented according to the following equation:<sup>36</sup>

$$I_i \propto |e_i \mathfrak{R} e_s|^2 \quad (2)$$

where  $e_i$  and  $e_s$  are the unit polarization vectors of the electric field for incident and scattered light, respectively. For the Raman setup used in this paper, the polarization vectors can be given as:

$$e_i^{\parallel} \begin{pmatrix} x & y & z \end{pmatrix} = \begin{pmatrix} 0 & 1 & 0 \end{pmatrix}; \quad e_s^{\parallel} \begin{pmatrix} x \\ y \\ z \end{pmatrix} = \begin{pmatrix} 0 \\ 1 \\ 0 \end{pmatrix}; \quad e_i^{\perp} \begin{pmatrix} x \\ y \\ z \end{pmatrix} = \begin{pmatrix} 1 \\ 0 \\ 0 \end{pmatrix}; \quad (3)$$

where the superscripts  $\parallel$  and  $\perp$  locate parallel and cross configurations of the Raman probe in the laboratory Cartesian frame  $(x, y, z)$ , respectively;  $\mathfrak{R}$ , a second-rank tensor depending on crystal structure, is usually referred to as the Raman scattering tensor of the vibrational mode under consideration. Loudon has computed the Raman tensors for the optical modes of the corundum structure, as follows:<sup>36</sup>

$$\mathfrak{R}_{A_g} = \begin{bmatrix} a & 0 & 0 \\ 0 & a & 0 \\ 0 & 0 & b \end{bmatrix}; \quad \mathfrak{R}_{E_g(X)} = \begin{bmatrix} c & 0 & 0 \\ 0 & -c & d \\ 0 & d & 0 \end{bmatrix}; \quad \mathfrak{R}_{E_g(Y)} = \begin{bmatrix} 0 & -c & -d \\ -c & 0 & 0 \\ -d & 0 & 0 \end{bmatrix} \quad (4)$$

where the constants  $a$ ,  $b$ ,  $c$ , and  $d$  represent the RTE of the crystal. Considering the Euler matrix,  $\Phi_{xyz}$ , and its inverse,  $\tilde{\Phi}_{xyz}$ , which can be used to transform the Cartesian coordinates  $(X, Y, Z)$  of the crystal into those of the laboratory frame  $(x, y, z)$ , a general expression for the Raman tensor of the  $k$ -th Raman band of the spectrum can be expressed as:

$$\mathfrak{R}_k(x, y, z) = \Phi(\theta, \varphi, \psi) \mathfrak{R}_k(X, Y, Z) \tilde{\Phi}(\theta, \varphi, \psi) \quad (5)$$

where the transformation matrices are defined in terms of three Euler angles  $(\theta, \varphi, \psi)$  in space (defined here as shown in Fig. 1(c)), as follows:

$$\Phi_{xyz} = \begin{pmatrix} \cos \theta \cos \varphi \cos \psi - \sin \varphi \sin \psi & \cos \theta \sin \varphi \cos \psi + \cos \varphi \sin \psi & -\sin \theta \cos \psi \\ -\sin \theta \cos \varphi - \cos \theta \cos \varphi \sin \psi & \cos \varphi \cos \psi - \cos \theta \sin \varphi \sin \psi & \sin \theta \sin \psi \\ \sin \theta \cos \varphi & \sin \theta \sin \varphi & \cos \theta \end{pmatrix} \quad (6)$$

$$\tilde{\Phi}_{xyz} = \begin{pmatrix} \cos \theta \cos \varphi \cos \psi - \sin \varphi \sin \psi & -\sin \theta \cos \varphi - \cos \theta \cos \varphi \sin \psi & \sin \theta \cos \varphi \\ \cos \theta \sin \varphi \cos \psi + \cos \varphi \sin \psi & \cos \varphi \cos \psi - \cos \theta \sin \varphi \sin \psi & \sin \theta \sin \varphi \\ -\sin \theta \cos \varphi & \sin \theta \sin \varphi & \cos \theta \end{pmatrix} \quad (7)$$

with  $0 \leq \theta \leq \pi$ ,  $0 \leq \varphi \leq 2\pi$ , and  $0 \leq \psi \leq 2\pi$ .

The general expression for the angular dependences on Euler angles of the intensities of the Raman active modes (i.e., in this case of the  $A_{1g}$  and  $E_g$  band intensities) can then be retrieved upon expanding Eq. (2) with substituting in it for Eqs. (3)-(7). By doing so, one might obtain a set of 6 independent equations expressing the expected Raman intensities produced by different vibrational modes as a function of the Euler angles in space, as follows:

$$I_{A_{1g}}^{\parallel} \propto [b \sin^2 \theta \sin^2 \psi + a(-\cos \psi \sin \varphi - \cos \theta \cos \varphi \sin \psi)^2] \quad (8)$$

$$+ a(\cos \varphi \cos \psi - \cos \theta \sin \varphi \sin \psi)^2 \quad (9)$$

$$I_{A_{1g}}^{\perp} \propto [(a-b) \sin^2 \theta \sin \psi \cos \psi]^2$$

$$I_{E_g(X)}^{\parallel} \propto \left\{ -\frac{c}{4} \cos 2\varphi [(3 + \cos 2\theta) \cos 2\psi + 2 \sin^2 \theta] - d \sin 2\theta \sin \varphi \sin^2 \psi + (d \cos \varphi \sin \theta + c \cos \theta \sin 2\varphi) \sin 2\psi \right\}^2 \quad (10)$$

$$I_{E_g(X)}^{\perp} \propto \left\{ -\cos 2\psi [d \cos \varphi \sin \theta + c \cos \theta \sin 2\varphi] - \frac{1}{4} [c(3 + \cos 2\theta) \cos 2\varphi - 2d \sin 2\theta \sin \varphi \sin 2\psi] \right\}^2 \quad (11)$$

$$I_{E_g(Y)}^{\parallel} \propto \left\{ 2(\cos \psi \sin \varphi + \cos \theta \cos \varphi \sin \psi) [c \cos \varphi \cos \psi + (d \sin \theta - c \cos \theta \sin \varphi) \sin \psi] \right\}^2 \quad (12)$$

$$I_{E_g(Y)}^{\perp} \propto \left\{ \frac{1}{2} [-2 \cos 2\psi (c \cos \theta \cos 2\varphi + d \sin \theta \sin \varphi) + \cos \varphi (-d \sin 2\theta \sin \varphi) \sin 2\psi] \right\}^2 \quad (13)$$

Note that the two distinct vibrational components of the intensity of the  $E_g$  mode, namely  $E_g(X)$  and  $E_g(Y)$ , can be linked to each other through the following equation:

$$I_{E_g}^{\parallel, \perp} = I_{E_g(X)}^{\parallel, \perp} + I_{E_g(Y)}^{\parallel, \perp} \quad (14)$$

In conclusion, Eqs. (8)-(14) represent the link between the irreducible representation of the crystal, given in Eq. (1), and the observable Raman intensity for the different vibrational

modes listed in it. This set of equations can be used either to calibrate the 4 RTE constants (i.e., through conducting polarized Raman experiments on known crystallographic planes) or to assess unknown crystallographic orientations, provided that the full set of RTE constants are known to a degree of precision.

## 2.2 The PDP formalism in the corundum structure and related calibrations

An arbitrary stress tensor,  $\sigma_{kl}$  (with  $k,l=x,y,z$ ), applied to a crystal in an arbitrary orthogonal reference frame (e.g., the laboratory reference frame) can be always transformed into an equivalent stress tensor,  $\sigma_{ij}$  (with  $i,j=1,2,3$ ), in the crystal reference frame (where the subscripts 1 and 3 locate the crystallographic  $a$ - and  $c$ -axis of the corundum structure, respectively). Such operation is conducted by means of tensorial rules of coordinate transformation, as follows:

$$\begin{bmatrix} \sigma_{11} & \sigma_{12} & \sigma_{13} \\ \sigma_{21} & \sigma_{22} & \sigma_{23} \\ \sigma_{31} & \sigma_{32} & \sigma_{33} \end{bmatrix} = \begin{bmatrix} \Phi_{11} & \Phi_{12} & \Phi_{13} \\ \Phi_{21} & \Phi_{22} & \Phi_{23} \\ \Phi_{31} & \Phi_{32} & \Phi_{33} \end{bmatrix} \begin{bmatrix} \sigma_{xx} & \sigma_{yy} & \sigma_{zz} \\ \sigma_{yx} & \sigma_{zy} & \sigma_{zx} \\ \sigma_{xy} & \sigma_{yz} & \sigma_{xz} \end{bmatrix} \begin{bmatrix} \Phi_{11} & \Phi_{12} & \Phi_{13} \\ \Phi_{21} & \Phi_{22} & \Phi_{23} \\ \Phi_{31} & \Phi_{32} & \Phi_{33} \end{bmatrix} \quad (15)$$

The tensorial relationship between strain and stress, applied along the principal crystallographic axes for the trigonal structure of sapphire, can be expressed according to the following tensorial equation:

$$\begin{pmatrix} \varepsilon_{11} \\ \varepsilon_{22} \\ \varepsilon_{33} \\ 2\varepsilon_{23} \\ 2\varepsilon_{13} \\ 2\varepsilon_{12} \end{pmatrix} = \begin{bmatrix} S_{11} & S_{12} & S_{13} & S_{14} & 0 & 0 \\ S_{12} & S_{11} & S_{13} & -S_{14} & 0 & 0 \\ S_{13} & S_{13} & S_{33} & 0 & 0 & 0 \\ S_{14} & -S_{14} & 0 & S_{44} & 0 & 0 \\ 0 & 0 & 0 & 0 & S_{44} & 2S_{14} \\ 0 & 0 & 0 & 0 & 2S_{14} & S_{66} \end{bmatrix} \begin{pmatrix} \sigma_{11} \\ \sigma_{22} \\ \sigma_{33} \\ \sigma_{23} \\ \sigma_{13} \\ \sigma_{12} \end{pmatrix} \quad (16)$$

where  $S_{ij}$  are the elastic compliance constants of the sapphire crystal, with values reported as:  $S_{11}=2.3 \times 10^{-12} \text{ Pa}^{-1}$ ,  $S_{12}=-0.7 \times 10^{-12} \text{ Pa}^{-1}$ ,  $S_{13}=-0.4 \times 10^{-12} \text{ Pa}^{-1}$ ,  $S_{33}=2.2 \times 10^{-12} \text{ Pa}^{-1}$ ,  $S_{44}=6.8 \times 10^{-12} \text{ Pa}^{-1}$ , and  $S_{14}=0.5 \times 10^{-12} \text{ Pa}^{-1}$ .<sup>37</sup>

Each vibrational mode,  $j$ , is associated with a frequency,  $\omega_j$ , and an effective force constant,  $K_j$ , which is the second derivative of the crystal potential energy with respect to mode normal coordinates.<sup>38</sup> However, stress/strain fields result in an alteration of the Raman frequencies of each vibrational mode in the crystal, due to the anharmonic nature of atomic interactions. The change in force constants under stress/strain can be represented by a matrix,  $[\Delta K]$ , whose size is in turn determined by the degeneracy of the Raman mode. The eigenvalues of the  $[\Delta K]$  matrix,  $\lambda$ , are related to Raman frequency shifts, as follows:

$$\lambda = \omega^2 - \omega_0^2 = (\omega + \omega_0)(\omega - \omega_0) = (\omega_0 + \omega - \omega_0 + \omega_0)(\omega - \omega_0) \approx 2\omega_0(\omega - \omega_0) \quad (17)$$

where  $\omega$  and  $\omega_0$  are the spectral positions under the stress field and that in the stress-free conditions, respectively, for the studied Raman band. Note that the band shift of any Raman mode caused by a stress perturbation is generally quite small (i.e.,  $\omega$  is close to the unperturbed one,  $\omega_0$ ), as compared to the wavenumber of the Raman band (i.e.,  $(\omega - \omega_0) \ll \omega_0$ ). Therefore, the higher-order terms in Eq. (17) can be neglected in first approximation. The value of  $\lambda$  can be obtained by solving the characteristic equation:

$$\det([\Delta K] - \lambda[I]) = 0 \quad (18)$$

where  $[I]$  is a unit diagonal matrix. The symmetry of the crystal under strain can be assessed with considering the symmetry elements common to the unstrained crystal and to the strain ellipsoid.<sup>39</sup> We mentioned above that, among the vibrational modes of sapphire, only two  $A_{1g}$  modes and five  $E_g$  modes are Raman active. Raman scatter thus allows a direct observation of both transverse and longitudinal optical phonons. Splitting and shift of a given energy level for an arbitrarily applied stress can be obtained by solving the eigenvalue problem for the crystal in the presence of a perturbing potential,  $V$ . Assuming the validity of the linear deformation potential theory,<sup>40</sup> the perturbing potential,  $V$ , is only proportional to terms linear in strain and, accordingly, is given by:

$$V = \sum_{i,j} V_{ij} \varepsilon_{ij}, \quad i, j = 1, 2, 3 \quad (19)$$

where  $V_{ij}$  is a symmetric second-rank tensor, whose terms are usually referred to as the deformation potentials. The representation generated by  $V_{ij}$  is:  $\Gamma_V = 2A_{1g} + 2E_g$ ; and, the components of the tensor operator,  $V_{ij}$ , can be grouped as follows:

$$V = \sum_{i,j} V_{ij} \varepsilon_{ij} = \frac{1}{2}(V_{11} + V_{22})(\varepsilon_{11} + \varepsilon_{22}) + V_{33} \varepsilon_{33} + \frac{1}{2}[(V_{11} - V_{22})(\varepsilon_{11} - \varepsilon_{22}) + V_{12} \varepsilon_{12}] + 2V_{13} \varepsilon_{13} + 2V_{23} \varepsilon_{23} \quad (20)$$

In Eq. (20),  $(V_{11} + V_{22})$  and  $V_{33}$  belong to  $A_{1g}$ ,  $(V_{11} - V_{22})$  and  $V_{13}$  belong to  $E_g(X)$ , and  $V_{12}$  and  $V_{23}$  belong to  $E_g(Y)$ , as can be seen from the basis functions appropriate for the representations of the  $A_{1g}$  and  $E_g$  modes of the  $D_{3d}$  point group (i.e., as listed in Table 1).

Under stress, the energy of a vibrational state belonging to  $A_{1g}$  will shift by an amount:

$$\frac{1}{2} \langle A_{1g} | V_{11} + V_{22} | A_{1g} \rangle (\varepsilon_{11} + \varepsilon_{22}) + \langle A_{1g} | V_{33} | A_{1g} \rangle \varepsilon_{33} \quad (21)$$

with the remaining terms vanishing according to the orthogonality theorem. Consequently, for the non-degenerated  $A_{1g}$  mode, Eq. (18) can be expressed as:

$$|K_1^A \varepsilon_{11} + K_2^A \varepsilon_{22} + K_3^A \varepsilon_{33} - \lambda| = 0 \quad (22)$$

According to Eqs. (17) and (22), the spectral shift of the  $A_{1g}$  mode is, therefore:

$$\Delta \omega_A = \omega_A - \omega_{0,A} = \frac{1}{2\omega_{0,A}} (K_1^A \varepsilon_{11} + K_2^A \varepsilon_{22} + K_3^A \varepsilon_{33}) \quad (23)$$

where  $K_1^A = K_2^A = \frac{1}{2} \langle A_{1g} | V_{11} + V_{22} | A_{1g} \rangle$  and  $K_3^A = \langle A_{1g} | V_{33} | A_{1g} \rangle$  are referred to as the PDP constants. Equations (16) and (23) can then be re-arranged to give:

$$\Delta \omega_A = \frac{1}{2\omega_{0,A}} \left[ (K_1^A S_{11} + K_2^A S_{12} + K_3^A S_{13}) \sigma_{11} + (K_2^A S_{11} + K_1^A S_{12} + K_3^A S_{13}) \sigma_{22} + (K_1^A S_{13} + K_2^A S_{13} + K_3^A S_{33}) \sigma_{33} \right] \quad (24)$$

According to Eqs. (6), (7), (15), and (24), the spectral shift of the Raman mode in response to stress in the laboratory reference frame can be explicitly expressed as:

$$\Delta \omega_A = \frac{1}{2\omega_{0,A}} \left\{ [(K_1^A S_{11} + K_2^A S_{12} + K_3^A S_{13})(\cos \theta \cos \varphi \cos \psi - \sin \psi \sin \varphi)^2 + (K_2^A S_{11} + K_1^A S_{12} + K_3^A S_{13})(\cos \psi \sin \varphi + \cos \theta \cos \varphi \sin \psi)^2 + (K_1^A S_{13} + K_2^A S_{13} + K_3^A S_{33}) \sin^2 \theta \cos^2 \varphi \right\} \sigma_{xx}$$

$$\begin{aligned}
& + \left[ (K_1^A S_{11} + K_2^A S_{12} + K_3^A S_{13})(-\sin 2\varphi \sin^2 \psi + \cos^2 \theta \sin 2\varphi \cos^2 \psi + \cos \theta \cos 2\varphi \sin 2\psi) \right. \\
& + (K_2^A S_{11} + K_1^A S_{12} + K_3^A S_{13})(\cos^2 \theta \sin 2\varphi \sin^2 \psi - \sin 2\varphi \cos^2 \psi - \cos \theta \cos 2\varphi \sin 2\psi) \\
& \left. + (K_1^A S_{13} + K_2^A S_{13} + K_3^A S_{33}) \cos^2 \theta \sin 2\varphi \right] \sigma_{xy} \\
& + \left[ (K_1^A S_{11} + K_2^A S_{12} + K_3^A S_{13})(\sin \varphi \sin \theta \sin 2\psi - \cos \varphi \sin 2\theta \cos^2 \psi) \right. \\
& + (K_2^A S_{11} + K_1^A S_{12} + K_3^A S_{13})(-\sin \varphi \sin \theta \sin 2\psi - \cos \varphi \sin 2\theta \sin^2 \psi) \\
& \left. + (K_1^A S_{13} + K_2^A S_{13} + K_3^A S_{33}) \cos \varphi \sin 2\theta \right] \sigma_{xz} \quad (25) \\
& + \left[ (K_1^A S_{11} + K_2^A S_{12} + K_3^A S_{13})(\cos \theta \sin \varphi \cos \psi + \sin \psi \cos \varphi)^2 \right. \\
& + (K_2^A S_{11} + K_1^A S_{12} + K_3^A S_{13})(-\cos \theta \cos \varphi \sin \psi + \cos \psi \sin \varphi)^2 \\
& \left. + (K_1^A S_{13} + K_2^A S_{13} + K_3^A S_{33}) \sin^2 \theta \sin^2 \varphi \right] \sigma_{yy} \\
& + \left[ (K_1^A S_{11} + K_2^A S_{12} + K_3^A S_{13})(-\cos \varphi \sin \theta \sin 2\psi - \sin \varphi \sin 2\theta \cos^2 \psi) \right. \\
& + (K_2^A S_{11} + K_1^A S_{12} + K_3^A S_{13})(\cos \varphi \sin \theta \sin 2\psi - \sin \varphi \sin 2\theta \sin^2 \psi) \\
& \left. + (K_1^A S_{13} + K_2^A S_{13} + K_3^A S_{33}) \sin \varphi \sin 2\theta \right] \sigma_{yz} \\
& + \left[ (K_1^A S_{11} + K_2^A S_{12} + K_3^A S_{13}) \sin^2 \theta \cos^2 \psi + (K_2^A S_{11} + K_1^A S_{12} + K_3^A S_{13}) \sin^2 \theta \sin^2 \psi \right. \\
& \left. + (K_1^A S_{13} + K_2^A S_{13} + K_3^A S_{33}) \cos^2 \theta \right] \sigma_{zz} \}
\end{aligned}$$

In order to express in close form the elements of the matrix  $V_{ij}$  for the doubly degenerate states  $X$  and  $Y$  of the  $E_g$  mode, a decomposition of the products of the basis functions of the class  $D_{3d}$  should preliminary be performed. Decomposition of the basis functions is given in Table 2.

**Table 2:** Decomposition of the products of the basis functions of the class  $D_{3d}$  needed to express in close form the elements of the matrix  $V_{ij}$  for the doubly degenerate states  $X$  and  $Y$  of the  $E_g$  mode. Here we assume:

$$\psi(A_{1g}) = \frac{X^2 + Y^2}{2}, \quad \psi_X(E_g) = \frac{X^2 - Y^2}{2}, \quad \psi_Y(E_g) = -XY$$

$D_{3d}$	$X$	$Y$
$X$	$\psi(A_{1g}) + \psi_X(E_g)$	$-\psi_Y(E_g)$
$Y$	$-\psi_Y(E_g)$	$\psi(A_{1g}) - \psi_X(E_g)$

Accordingly, the secular equation for the  $E_g$  mode can be expressed in terms of PDP constants,  $K_1^E, K_2^E, K_3^E$  and  $K_4^E$ , as follows:

$$\begin{vmatrix}
K_1^E(\epsilon_{11} + \epsilon_{22}) + K_2^E \epsilon_{33} + K_3^E(\epsilon_{11} - \epsilon_{22}) + K_4^E \epsilon_{13} - \lambda & K_3^E \epsilon_{12} + K_4^E \epsilon_{23} \\
K_3^E \epsilon_{12} + K_4^E \epsilon_{23} & K_1^E(\epsilon_{11} + \epsilon_{22}) + K_2^E \epsilon_{33} - K_3^E(\epsilon_{11} - \epsilon_{22}) - K_4^E \epsilon_{13} - \lambda
\end{vmatrix} = 0 \quad (26)$$

where:

$$K_1^E = \frac{1}{2} \langle \psi(A_{1g}) | V_{11} + V_{22} \rangle \quad (27)$$

$$K_2^E = \langle \psi(A_{1g}) | V_{33} \rangle, \quad K_3^E = \frac{1}{2} \langle \psi_X(E_g) | V_{11} - V_{22} \rangle = \frac{1}{2} \langle \psi_Y(E_g) | V_{12} \rangle \quad (28)$$

$$K_4^E = 2 \langle \psi_X(E_g) | V_{13} \rangle = 2 \langle \psi_Y(E_g) | V_{23} \rangle \quad (29)$$

According to Eqs. (17) and (26), the spectral shift can be expressed as:

$$\begin{aligned}
\Delta \omega_{E(X,Y)} &= \omega_{E(X,Y)} - \omega_{0,E(X,Y)} \quad (30) \\
&= \frac{1}{2\omega_{0,E(X,Y)}} \left[ K_1^E(\epsilon_{11} + \epsilon_{22}) + K_2^E \epsilon_{33} \pm \sqrt{\left[ K_3^E(\epsilon_{11} - \epsilon_{22}) + K_4^E \epsilon_{13} \right]^2 + \left( K_3^E \epsilon_{12} + K_4^E \epsilon_{23} \right)^2} \right]
\end{aligned}$$

By considering the relationship between strain and stress in Eq. (16), Eq. (30) can be rewritten, as follows:

$$\begin{aligned}
\Delta \omega_{E(X,Y)} &= \frac{1}{2\omega_{0,E}} \left\{ \left[ K_1^E(S_{11} + S_{12}) + K_2^E S_{13} \right] (\sigma_{11} + \sigma_{22}) + (2K_1^E S_{13} + K_2^E S_{33}) \sigma_{33} \right. \\
&\quad \left. \pm \left[ K_3^E(S_{11} - S_{12})(\sigma_{11} - \sigma_{22}) + K_4^E(S_{44}\sigma_{13} + 2S_{14}\sigma_{12}) \right]^2 \right. \\
&\quad \left. + \left\{ 2K_3^E[S_{14}\sigma_{13} + (S_{11} - S_{12})\sigma_{12}] + K_4^E[S_{14}(\sigma_{11} - \sigma_{22}) + S_{44}\sigma_{23}] \right\}^2 \right\}^{\frac{1}{2}} \quad (31)
\end{aligned}$$

The overall peak shift of the combined signal can be set as the average of individual peak-shifts weighted by their relative intensities:

$$\Delta \bar{\omega} = \frac{\sum_{i=1}^2 (I_i \Delta \omega_i)}{\sum_{i=1}^2 I_i} \quad (32)$$

For the cases of cross and parallel polarization, Eq. (32) can be rewritten as:

$$\Delta \bar{\omega}_E^{\perp\perp} = \frac{\Delta \omega_X I_{E_g(X)}^{\perp\perp} + \Delta \omega_Y I_{E_g(Y)}^{\perp\perp}}{I_{E_g(X)}^{\perp\perp} + I_{E_g(Y)}^{\perp\perp}} \quad (33)$$

which can in turn be expanded into:

$$\begin{aligned}
\Delta \bar{\omega}_E^{\perp\perp} &= \frac{1}{2\omega_{0,E}} \left\{ \left[ K_1^E(S_{11} + S_{12}) + K_2^E S_{13} \right] (\sigma_{11} + \sigma_{22}) + (2K_1^E S_{13} + K_2^E S_{33}) \sigma_{33} \right. \\
&\quad + \frac{I_{E_g(X)}^{\perp\perp} - I_{E_g(Y)}^{\perp\perp}}{2\omega_{0,E} (I_{E_g(X)}^{\perp\perp} + I_{E_g(Y)}^{\perp\perp})} \left\{ \left[ K_3^E(S_{11} - S_{12})(\sigma_{11} - \sigma_{22}) + K_4^E(S_{44}\sigma_{13} + 2S_{14}\sigma_{12}) \right]^2 \right. \\
&\quad \left. + \left\{ 2K_3^E[S_{14}\sigma_{13} + (S_{11} - S_{12})\sigma_{12}] + K_4^E[S_{14}(\sigma_{11} - \sigma_{22}) + S_{44}\sigma_{23}] \right\}^2 \right\}^{\frac{1}{2}} \quad (34)
\end{aligned}$$

or, in the laboratory reference frame:

$$\begin{aligned}
\Delta \bar{\omega}_E^{\perp\perp} &= \frac{1}{2\omega_{0,E}} \left\{ \left[ K_1^E(S_{11} + S_{12}) + K_2^E S_{13} \right] \left[ \sigma_{xx}(\cos^2 \theta \cos^2 \varphi + \sin^2 \varphi) + \sigma_{yy}(-\sin 2\varphi + \cos^2 \theta \sin 2\varphi) \right. \right. \\
&\quad \left. \left. + \sigma_{zz}(-\cos \varphi \sin 2\theta) + \sigma_{yy}(\cos^2 \theta + 1)(\sin^2 \varphi \cos^2 \psi + \cos^2 \theta \sin^2 \varphi) + \sigma_{yz}(-\sin \varphi \sin 2\theta) + \sigma_{zz} \sin^2 \theta \right] \right. \\
&\quad \left. + (2K_1^E S_{13} + K_2^E S_{33}) \left[ \sigma_{xx} \sin^2 \theta \cos^2 \varphi + \sigma_{yy} \cos^2 \theta \sin 2\varphi + \sigma_{zz} \cos \varphi \sin 2\theta + \sigma_{yy} \sin^2 \theta \sin^2 \varphi \right. \right. \\
&\quad \left. \left. + \sigma_{yz} \sin \varphi \sin 2\theta + \sigma_{zz} \cos^2 \theta \right] \right. \\
&\quad + \frac{I_{E_g(X)}^{\perp\perp} - I_{E_g(Y)}^{\perp\perp}}{I_{E_g(X)}^{\perp\perp} + I_{E_g(Y)}^{\perp\perp}} \times \left\{ \left[ K_3^E(S_{11} - S_{12}) \left\{ \sigma_{xx}(\cos^2 \theta \cos^2 \varphi \cos 2\psi - \cos 2\psi \sin^2 \varphi - \sin 2\varphi \cos \theta \sin 2\psi) \right. \right. \right. \\
&\quad \left. \left. + \sigma_{yy}(\sin 2\varphi \cos 2\psi(1 + \cos^2 \theta) + 2\cos \theta \cos 2\varphi \sin 2\psi) + \sigma_{zz}(2\sin \varphi \sin \theta \sin 2\psi - \cos \varphi \sin 2\theta \cos 2\psi) \right. \right. \\
&\quad \left. \left. + \sigma_{yy}[(\cos^2 \theta - 1)(\sin^2 \varphi \cos^2 \psi + \sin^2 \psi \cos^2 \varphi) + \cos \theta \sin 2\psi \sin 2\varphi] \right. \right. \\
&\quad \left. \left. + \sigma_{yz}(-2\cos \varphi \sin \theta \sin 2\psi - \sin \varphi \sin 2\theta \cos 2\psi) + \sigma_{zz} \sin^2 \theta \cos 2\psi \right\} \right. \\
&\quad \left. + K_4^E \left\{ S_{44} \left[ \sigma_{xx}[\cos \theta \sin \theta \cos^2 \varphi \cos \psi - \sin \theta \cos \varphi \sin \theta \sin \psi] + \sigma_{yy}[\cos \theta \sin \theta \sin 2\varphi \cos \psi + \sin \theta \cos 2\varphi \sin \psi] \right. \right. \right. \\
&\quad \left. \left. + \sigma_{zz}(\cos 2\theta \cos \varphi \cos \psi - \cos \theta \sin \varphi \sin \psi) + \sigma_{yy}[\cos \theta \sin \theta \sin^2 \varphi \cos \psi + \sin \theta \sin \varphi \cos \varphi \sin \psi] \right. \right. \\
&\quad \left. \left. + \sigma_{yz}(\cos 2\theta \sin \varphi \cos \psi + \cos \theta \cos \varphi \sin \psi) - \sigma_{zz} \cos \theta \sin \theta \cos \psi \right\} \right. \\
&\quad \left. + 2S_{14} \left\{ \sigma_{xx}[(\sin^2 \varphi - \cos^2 \theta \cos^2 \varphi) \sin \psi \cos \psi - \cos \theta \sin \varphi \cos \varphi \cos 2\psi] \right. \right. \\
&\quad \left. \left. + \sigma_{yy}[\cos \theta \cos 2\varphi \cos 2\psi - \sin 2\varphi \sin \psi \cos \psi(1 + \cos^2 \theta)] + \sigma_{zz}(\cos \varphi \sin 2\theta \sin \psi \cos \psi + \sin \varphi \sin \theta \cos 2\psi) \right. \right. \\
&\quad \left. \left. + \sigma_{yy}[\cos \theta \sin \varphi \cos \varphi \cos 2\psi + \sin \psi \cos \psi(\cos^2 \varphi - \cos^2 \theta \sin^2 \varphi)] \right. \right. \\
&\quad \left. \left. + \sigma_{yz}(\sin \varphi \sin 2\theta \sin \psi \cos \psi - \cos \varphi \sin \theta \cos 2\psi) - \sigma_{zz} \sin^2 \theta \sin \psi \cos \psi \right\}^2 \right. \\
&\quad \left. + \left\{ 2K_3^E \left[ S_{14} \left\{ \sigma_{xx}[\cos \theta \sin \theta \cos^2 \varphi \cos \psi - \sin \theta \cos \varphi \sin \theta \sin \psi] \right. \right. \right. \right. \\
&\quad \left. \left. + \sigma_{yy}[\cos \theta \sin \theta \sin 2\varphi \cos \psi + \sin \theta \cos 2\varphi \sin \psi] + \sigma_{zz}(\cos 2\theta \cos \varphi \cos \psi - \cos \theta \sin \varphi \sin \psi) \right. \right. \\
&\quad \left. \left. + \sigma_{yy}[\cos \theta \sin \theta \sin^2 \varphi \cos \psi + \sin \theta \sin \varphi \cos \varphi \sin \psi] + \sigma_{yz}(\cos 2\theta \sin \varphi \cos \psi + \cos \theta \cos \varphi \sin \psi) \right. \right. \\
&\quad \left. \left. - \sigma_{zz} \cos \theta \sin \theta \cos \psi \right\} \right.
\end{aligned} \quad (35)$$

$$\begin{aligned}
& + (S_{11} - S_{12}) \left\{ \sigma_{xx} \left[ (\sin^2 \varphi - \cos^2 \theta \cos^2 \varphi) \sin \psi \cos \psi - \cos \theta \sin \varphi \cos \varphi \cos 2\psi \right] \right. \\
& + \sigma_{yy} \left[ \cos \theta \cos 2\varphi \cos 2\psi - \sin 2\varphi \sin \psi \cos \psi (1 + \cos^2 \theta) \right] + \sigma_{xz} (\cos \varphi \sin 2\theta \sin \psi \cos \psi + \sin \varphi \sin \theta \cos 2\psi) \\
& + \sigma_{yz} \left[ \cos \theta \sin \varphi \cos \varphi \cos 2\psi + \sin \psi \cos \psi (\cos^2 \varphi - \cos^2 \theta \sin^2 \varphi) \right] \\
& + \sigma_{zz} (\sin \varphi \sin 2\theta \sin \psi \cos \psi - \cos \varphi \sin \theta \cos 2\psi) - \sigma_{xx} \sin^2 \theta \sin \psi \cos \psi \left. \right\} \\
& + K_4^E \left\{ S_{14} \left[ \sigma_{xx} (\cos^2 \theta \cos^2 \varphi \cos 2\psi - \cos 2\psi \sin^2 \varphi - \sin 2\varphi \cos \theta \sin 2\psi) \right. \right. \\
& + \sigma_{yy} (\sin 2\varphi \cos 2\psi (1 + \cos^2 \theta) + 2 \cos \theta \cos 2\varphi \sin 2\psi) + \sigma_{xz} (2 \sin \varphi \sin \theta \sin 2\psi - \cos \varphi \sin 2\theta \cos 2\psi) \\
& + \sigma_{yz} \left. \left. \left[ (\cos^2 \theta - 1) (\sin^2 \varphi \cos^2 \psi + \sin^2 \psi \cos^2 \varphi) + \cos \theta \sin 2\psi \sin 2\varphi \right] \right. \right. \\
& + \sigma_{zz} (-2 \cos \varphi \sin \theta \sin 2\psi - \sin \varphi \sin 2\theta \cos 2\psi) + \sigma_{xx} \sin^2 \theta \cos 2\psi \left. \right\} \\
& + S_{44} \left\{ \sigma_{xx} \left[ -\cos \theta \sin \theta \cos^2 \varphi \sin \psi - \sin \theta \cos \varphi \sin \varphi \cos \psi \right] + \sigma_{yy} \left[ -\cos \theta \sin \theta \sin 2\varphi \sin \psi + \sin \theta \cos 2\varphi \cos \psi \right] \right. \\
& + \sigma_{xz} (-\cos 2\theta \cos \varphi \sin \psi - \cos \theta \sin \varphi \cos \psi) + \sigma_{yz} \left. \left. \left[ -\cos \theta \sin \theta \sin^2 \varphi \sin \psi + \sin \theta \sin \varphi \cos \varphi \cos \psi \right] \right. \right. \\
& + \sigma_{zz} (-\cos 2\theta \sin \varphi \sin \psi + \cos \theta \cos \varphi \cos \psi) + \sigma_{xx} \cos \theta \sin \theta \sin \psi \left. \left. \right\} \right\}^2 \left. \right\}^{\frac{1}{2}}
\end{aligned}$$

As described in the previous section, local information of crystal orientation in the sample (i.e., the local values of the Euler angles,  $(\theta, \varphi, \psi)$ ) can be retrieved from the angular dependences of experimentally obtained polarized Raman intensities. Such crystallographic assessments requires the knowledge of the full set of RTE and the collection of a set of polarized Raman spectra as a function of in-plane rotation angle in backscattered configuration. Based on this knowledge, a tensorial algorithm built on Eqs. (25) and (35) and applied to different bands could be obtained, with the related Euler angles determined from best fitting the measured intensity variations as a function of in-plane rotation angle (i.e., according to Eqs. (8)-(14)). The structure of this algorithm is explained in the following section.

### 2.3 Algorithm for vibrational stress analysis in polycrystalline samples.

In introducing the vibrational spectrum of sapphire in Fig. 2, we have pointed out at the outset the availability of more than six independent bands, which is a fundamental prerequisite for the viability of our method of tensor-resolved stress analyses. Three-dimensional stress analyses indeed involve the determination of six independent stress tensor components from each Raman spectral measurement. In practice, the knowledge of the PDP constants for the different vibrational modes belonging to the irreducible representation enables one to set a system of six independent equations, which relates the observed spectral shifts to the six independent components of the stress tensor through Eqs. (25) and (35). The analytical expansion of this procedure is somewhat cumbersome and it is not explicitly shown here. In this context, we shall limit our treatment to explicitly discuss the method for setting the system of working equations, while leaving the overall algorithm to be solved case-by-case through a numerical computational routine. Each individual Raman band of the corundum structure obeys a different set of PDP constants depending on its belonging to the  $A_{1g}$  or  $E_g$  families of vibrational modes, and experiences a different spectral shift in response to a given stress tensor:  $\Delta\omega_i = f_i(\sigma_{xx}, \sigma_{yy}, \sigma_{xz}, \sigma_{yz}, \sigma_{zz})$  (cf. Eqs. (25) and (35), for  $A_{1g}$  and  $E_g$  modes, respectively). As a result, a system of at least six independent linear equations can be obtained. Each equation can be either Eq. (25) or Eq. (35), depending on the band examined, and relates the stress tensor components to the observed Raman shifts, as follows:

$$\begin{cases} \Delta\omega_1 = f_1(\theta, \varphi, \psi, \sigma_{xx}, \sigma_{yy}, \sigma_{xz}, \sigma_{yz}, \sigma_{zz}) \\ \Delta\omega_2 = f_2(\theta, \varphi, \psi, \sigma_{xx}, \sigma_{yy}, \sigma_{xz}, \sigma_{yz}, \sigma_{zz}) \\ \dots\dots\dots \\ \Delta\omega_i = f_i(\theta, \varphi, \psi, \sigma_{xx}, \sigma_{yy}, \sigma_{xz}, \sigma_{yz}, \sigma_{zz}) \\ \dots\dots\dots \\ \Delta\omega_6 = f_6(\theta, \varphi, \psi, \sigma_{xx}, \sigma_{yy}, \sigma_{xz}, \sigma_{yz}, \sigma_{zz}) \end{cases} \quad (36)$$

The system of Eq. (36) can in turn be reversed to give the full set of components of the stress tensor as a function of the 6 independent spectral shifts,  $\Delta\omega_i$ , experimentally observed (i.e., a string of known parameters) and 3 Euler angles in space. The reversed system of equations can thus be set, as follows:

$$\begin{cases} \sigma_{xx} = g_1(\theta, \varphi, \psi, \Delta\omega_1, \Delta\omega_2, \Delta\omega_3, \Delta\omega_4, \Delta\omega_5, \Delta\omega_6) \\ \sigma_{yy} = g_2(\theta, \varphi, \psi, \Delta\omega_1, \Delta\omega_2, \Delta\omega_3, \Delta\omega_4, \Delta\omega_5, \Delta\omega_6) \\ \sigma_{xz} = g_3(\theta, \varphi, \psi, \Delta\omega_1, \Delta\omega_2, \Delta\omega_3, \Delta\omega_4, \Delta\omega_5, \Delta\omega_6) \\ \sigma_{yz} = g_4(\theta, \varphi, \psi, \Delta\omega_1, \Delta\omega_2, \Delta\omega_3, \Delta\omega_4, \Delta\omega_5, \Delta\omega_6) \\ \sigma_{zz} = g_5(\theta, \varphi, \psi, \Delta\omega_1, \Delta\omega_2, \Delta\omega_3, \Delta\omega_4, \Delta\omega_5, \Delta\omega_6) \\ \sigma_{zz} = g_6(\theta, \varphi, \psi, \Delta\omega_1, \Delta\omega_2, \Delta\omega_3, \Delta\omega_4, \Delta\omega_5, \Delta\omega_6) \end{cases} \quad (37)$$

Note that reversing the system of Eq. (36) into Eq. (37) does not alter the linearity of the equations, for which, therefore, a unique solution should exist. The solution to Eq. (37) can become available with the aid of a computing program set with commercially available computational software. From a conceptual viewpoint, for making it possible the determination of individual stress tensor components according to the above approach, two sets of parameters, one of extrinsic nature (i.e., the local values of three Euler angles at each location of recorded Raman spectrum) and the other intrinsic to the crystal structure (the full set of PDP for each selected Raman band), must become available. The former set of parameters is needed to correlate the Cartesian reference frame of the crystal axes to that of the laboratory axes. The local sets of Euler angular values should then be retrieved through Eqs. (8)-(14) from polarized Raman intensity values of selected bands whose shifts are then used for stress analysis. So far, the suggested procedure appears to be exactly the same for both single-crystalline and polycrystalline samples. However, in the case of polycrystalline samples, the set of Euler angles in space is obviously different at each measurement location and, therefore, the algorithm requires in-plane rotational experiments at each measurement point for determining the local set of  $\theta$ ,  $\varphi$ , and  $\psi$  values. Accordingly, the formalism requires the introduction of a set of local Cartesian variables, as follows:

$$\sigma_{ij}(x, y, z) = g_k[\theta(x, y, z), \varphi(x, y, z), \psi(x, y, z), \Delta\omega_l]$$

where the indices  $i, j = x, y, z$ ; and  $k, l = 1, 2, \dots, 6$ . Note that the proposed extension to polycrystalline samples through Eq. (38), except for the increased cumbersomeness of the computational routine, does not involve any conceptual difference as compared to the case of single-crystalline samples. However, a conceptually important difference arises when the effect of the finite size of the Raman probe is considered, which has to be incorporated into the computational algorithm. These additional aspects of the stress computational problem are discussed in the next section.

## 2.4 Probe response functions for Raman and fluorescence bands.

In practical Raman and fluorescence measurements, substantial penetration of the incident monochromatic light may occur as a consequence of the transparency of the investigated material (i.e., as in the case of both sapphire and polycrystalline  $\text{Al}_2\text{O}_3$ ). Accordingly, the Raman spectrum collected at a (nominal) geometrical location  $(x_0, y_0, z_0)$  is also contributed by spectral components originating from neighboring regions of the sample belonging to a finite volume around such nominal location. There are two practical consequences in having a finite dimension of the probe: (i) in polycrystalline samples structured as grains assembly, the crystallographic orientation read by the probe is an averaged one among the population of grains present in the probe; and, (ii) in highly graded stress fields, the obtained stress information is averaged over the finite probe volume, and thus the stress magnitude read by the probe could be underestimated as compared to the real one (i.e., the larger the probe, the larger the underestimation). Note that the above item (i) only applies to Raman spectroscopic assessments, while fluorescence spectra are conspicuously unaffected by crystal orientation. The stress averaging effect described in (ii) occurs in both types of measurement. The contributions to the local spectrum from different locations within the probe can be represented by a probe response function (PRF), which describes the intensity of light scattered from a given point  $(x, y, z)$  when the incident beam is focused at the geometrical center  $(x_0, y_0, z_0)$ . A mathematical form for the PRF in space, common to Raman and fluorescence probes, can be given, as follows:<sup>41-43</sup>

$$G(x, y, z; x_0, y_0, z_0) \propto \exp\left[-2\frac{(x-x_0)^2 + (y-y_0)^2}{B^2}\right] \times \left[\frac{p^2}{(z-z_0)^2 + p^2} \exp(-2\alpha_{\text{eff}}z)\right] \quad (39)$$

where  $B$  is the diameter of the laser beam at its waist in the focal plane,  $p$  is the so-called in-depth probe response parameter, which for an unfocused beam tends to infinity, and  $\alpha_{\text{eff}}$  is the effective absorption coefficient of the material at the incident wavelength. This latter parameter might differ from the commonly defined absorption coefficient,  $\alpha$ , because of the influence of grain boundaries, which leads to a dependence on grain size in polycrystalline samples.<sup>28</sup> In order to obtain a complete description of the observed Raman or fluorescence spectrum, a convolution of infinitesimal spectral contributions,  $I_{\text{obs}}(\omega)$ , originating from each location in the sample within the probe volume, must be considered. Accordingly, the intensity of the emitted signal can be described according to the following equation:

$$I_{\text{obs}}(\omega) \propto \int_{-\infty}^{+\infty} \int_{-\infty}^{+\infty} \int_0^{+\infty} I(\omega) \times \exp\left[-2\frac{(x-x_0)^2 + (y-y_0)^2}{B^2}\right] \times \frac{p^2}{(z-z_0)^2 + p^2} \left[\exp(-2\alpha_{\text{eff}}z)\right] dx dy dz \quad (40)$$

where  $I(\omega)$  is the local Raman fluorescence line shape, which, for a polycrystalline sample containing an inhomogeneous stress distribution inside the probe volume, is in turn a function of both local crystal orientation and stress field. If the spectral shift of the selected Raman band in presence of stress,  $\Delta\omega = \omega - \omega_0$ , (i.e., with  $\omega$  and  $\omega_0$  being the frequencies at band maximum in presence and in absence of stress, respectively) can be found negligible with respect to the overall spectroscopic band width,  $W$  (i.e.,  $(\omega - \omega_0)^2 \ll W^2$ ), then the observed band shift can be expressed to a degree of precision through an average of spectral shift values weighted by the

effective scattered intensity at the irradiated point. In other words, the observed band shift,  $\Delta\omega_{\text{obs}}(x_0, y_0, z_0)$ , can be calculated by using the PRF as a weighting function in adding the local band shifts,  $\Delta\omega(x, y, z)$ , collected within the probe, as follows:

$$\Delta\omega_{\text{obs}}(x_0, y_0, z_0) = \frac{\int_{-\infty}^{\infty} \int_{-\infty}^{\infty} \int_0^{\infty} G(x, y, z; x_0, y_0, z_0) \Delta\omega(x, y, z) dx dy dz}{\int_{-\infty}^{\infty} \int_{-\infty}^{\infty} \int_0^{\infty} G(x, y, z; x_0, y_0, z_0) dx dy dz} \quad (41)$$

Equation (41) can easily be solved through numerical routines and with the aid of commercially available computing software,<sup>44</sup> provided that the local spectral shift at any given location  $(x, y, z)$  in presence of stress is known. Note, however, that the inverse procedure, namely a deconvolution routine using Eq. (41) involves the solution of an inverse integral

equation whose unknown function,  $\Delta\omega(x, y, z)$ , lies in the argument of a triple integral. The solution for such equation is not unique unless the ‘‘character’’ of the unknown function can be guessed *a priori* or the morphology of the convoluted function (experimentally retrieved) can be assumed to yet retain the ‘‘character’’ of the native function and used as a trial function.

A further complication, although only peculiar to Raman assessments, resides in the fact that the crystallographic orientation probed in a polycrystalline sample will depend on the relative volume ratio between probe and grains. In other words, the statistical number of grains of the polycrystalline structure contained in the probe will determine the experimental output in terms of Eqs. (8)-(14) at a given location. The Raman probe in the polycrystal will thus display a spectrum affected not only by the orientation of each grain comprised in its volume, but also by the statistical fraction of grains with the same orientation. A schematic draft showing the interaction between the Raman probe and the microstructural arrangement in a polycrystalline sample is shown in Fig. 3. One limit case would be that the probe volume is appreciably smaller than the average grain size (Fig. 3(a)). In this case, an application of the selection rules Eqs. (8)-(14) will simply lead to the determination of the crystallographic orientation of the single grain probed. The other limit case is that the probe contains a number of grains large enough to justify, in the absence of textures in the polycrystal, the assumption that all the possible orientations are equally represented in the probe and the average orientation can be considered fully random (Fig. 3(c)). In this latter case, no angular dependence should be found for any Raman band upon in-plane rotation. In engineering applications, the grain size of the  $\text{Al}_2\text{O}_3$  polycrystals is typically in the order of 1  $\mu\text{m}$ . Considering the relatively high transparency of the  $\text{Al}_2\text{O}_3$  lattice to visible light, one should expect that at least several grains fall in the volume of a confocal Raman microprobe (a more precise estimation will be given in a forthcoming section). Therefore, the general case of interest in engineering applications typically lies in an intermediate geometry between the two above-mentioned limit cases (Fig. 3(b)). When only few grains are comprised in the probe, the selection rules still apply locally. But, in-plane rotation experiments and the application of Eqs. (8)-(14) only lead to an (PRF-weighted) average set of orientation angles. In textured polycrystals, algorithms based on orientation distribution functions have been applied to retrieve the population of axial orientation diverging from the average orientation axis of the textured structure.<sup>20,45</sup> However, in the presence of a limited number of randomly oriented grains, a

deconvolution of the individual grain contributions cannot easily be achieved. From a computational point of view, there can be many different combinations of Euler angles that give the same angular dependences, and the solution is not unique. One possibility to bypass this difficulty and proceed forward with the computational algorithm is to consider the unitary volume of the Raman probe as a “crystal” (or a single “grain”) with orientation corresponding to the measured average orientation. This means that the probed sample becomes composed of an ensemble of single-crystalline entities that can be referred to as “mesocrystals”. Obviously, this approach represents an approximation, but the error involved with it decreases with decreasing the probe volume, ultimately reaching an exact solution when the probe size is smaller than the grain size of the polycrystalline sample.

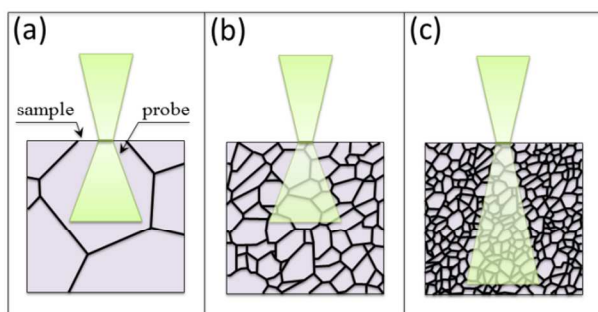


**Fig. 3:** Draft showing the interaction between Raman probe and the microstructural arrangement in a polycrystalline sample: (a) probe volume appreciably smaller than the grain size; (b) probe volume comprising only few grains that determine an average orientation; and, (c) probe volume containing a large number of randomly oriented grains.

### 3. Experimental procedures

All the Raman spectroscopic experiments described in this paper were carried out in a backscattering configuration with using a triple monochromator (T-64000, Horiba/Jobin-Yvon, Kyoto – Japan) equipped with liquid nitrogen-cooled charge coupled device (CCD), a confocal pinhole and polarization filters. The excitation source in the present experiments used the 488 nm line of an Ar-ion laser (Stabilite 2017, Spectra-Physics, Mountain View – CA). An objective lens with a numerical aperture of 0.5 was used both to focus the laser beam on the sample surface and to collect the scattered Raman spectra. All the confocal experiments described in this paper were conducted with a pinhole aperture of 100  $\mu\text{m}$  and with employing an objective lens of magnification 100x. The laser power was 200 mW and the exposure time was 60 s for collecting one Raman spectrum. Influence of thermal heating caused by laser irradiation for long-time accumulation on the Raman spectrum has been found negligible by using standard silicon. With the aid of a rotating goniometer jig, spectral positions and intensities of Raman bands were monitored upon rotating the sample under polarized light in parallel and cross configurations. Spectral Raman lines were analyzed using a commercially available software package (Labspec 4.02, Horiba/Jobin-Yvon, Kyoto - Japan). Fitting was performed according to Gaussian-Lorentzian functions after subtracting a linear baseline. All mathematical procedures were carried out with the aid of commercially available computational software.<sup>44</sup>

Bending bars obtained from four different sapphire single-crystalline samples with different orientations were loaded in a four-point flexure jig (upper and lower span equal to 15 and 30 mm, respectively), with outer fiber tensile face corresponding to their  $(\bar{1}\bar{1}02)$ ,  $(1\bar{1}\bar{2}0)$ ,  $(0001)$ , and  $(10\bar{1}0)$  planes (i.e., the  $R$ ,  $a$ ,  $c$ , and  $m$  crystallographic planes, respectively). All samples were cleaved and machined commercially available crystals (manufactured by Kyocera, Co., Tokyo, Japan). Prior to spectroscopic characterizations, the samples were polished with fine diamond paste (0.1  $\mu\text{m}$ ) and then annealed, in order to minimize the effect of residual stresses due to crystal growth, cleavage, and subsequent surface machining. A fine-grained polycrystalline alumina sample (99.9 wt% pure; SSA-999W grade, Nikkato Corp., Osaka, Japan) was also used for Raman calibrations.

Raman and fluorescence spectroscopic tests were also applied to a sample made of two  $\text{Al}_2\text{O}_3$  polycrystalline blocks, which were joined to a Ni/Mo/Nb/Mo/Ni interlayer (125- $\mu\text{m}$ -thick Nb core, 2- $\mu\text{m}$ -thick Mo coating, and 2  $\mu\text{m}$ -thick Ni cladding). The joint was obtained by loading into a graphite-element hot-pressing furnace and processed under high vacuum (6 h at 1400°C under a constant pressure of 2.4 MPa). The polycrystalline alumina block consisted of the same commercially available high-purity  $\text{Al}_2\text{O}_3$  material mentioned above in the morphology of a 20 x 20 x 20 mm parallelepiped. Before joining with the metal, the face of the  $\text{Al}_2\text{O}_3$  block was first ground and subsequently polished using fine grit diamond suspensions down to 1  $\mu\text{m}$ . A final polishing procedure was made with a colloidal-silica suspension.

## 4. Results and discussion

### 4.1 Determination of RTE constants by rotation measurements.

Equations (8)-(14) were applied to in-plane rotation experiments conducted on different crystallographic planes of sapphire single-crystal. Our choice of Euler angles and Cartesian coordinates with respect to the corundum structure is schematically shown in Fig. 1(c). The scattered Raman intensity was recorded as a function of the in-plane rotation angle on the  $c$ -plane ( $\theta=0$ ;  $\varphi=0$ ), the  $a$ -plane ( $\theta=\frac{\pi}{2}$ ;  $\varphi=0$ ), the  $m$ -plane ( $\theta=\frac{\pi}{2}$ ;  $\varphi=\frac{\pi}{2}$ ), and the  $R$ -plane ( $\theta=\frac{58\pi}{180}$ ;  $\varphi=\frac{\pi}{2}$ ). Specification of the Euler angles, as shown in brackets, for each crystallographic plane under investigation leads to a set of predictive equations giving the dependence of the Raman intensity on the in-plane rotation angle,  $\psi$ . Such equations can be used as trial functions to determine, through a best-fitting routine on the experimental data, the full set of 4 RTE constants for sapphire.

In the present study, the Raman tensor elements  $a$ ,  $b$ ,  $c$ , and  $d$  were determined from the measured intensity variations of the 378 and 418  $\text{cm}^{-1}$  bands (belonging to  $E_g$  and  $A_{1g}$  modes, respectively; cf. Figs. 1(b) and 2) as a function of rotation angle,  $\psi$ . Figures 4(a)-(h) represent selected angular dependencies and the respective best-fitting curves for the modes  $I_{A_{1g}}^{\square}$ ,  $I_{A_{1g}}^{\perp}$ ,  $I_{E_g}^{\square}$ , and  $I_{E_g}^{\perp}$  in the  $a$ - and in the  $R$ -plane. According to Eqs. (8)-(14), the full set of RTE constants could be obtained from (polarized) angular rotation experiments conducted on all crystallographic planes, except for the  $c$ -plane (from which the tensor elements  $a$ - $d$  are not accessible). Confirmation of RTE

results could be obtained by comparing fitting data collected as a function of rotation angle,  $\psi$ , on different crystallographic planes in parallel or cross configurations. Least square method was applied here to best fit the experimental data shown in Fig. (4) by using Eqs. (8)-(14). A minimum value of the deviation (i.e., mean square error) could be retrieved accordingly. As a general output, the experimental data fitted the theoretical predictions to a good degree of precision in both cases of parallel and cross modes, although a higher data scatter could be found on same specific plane.

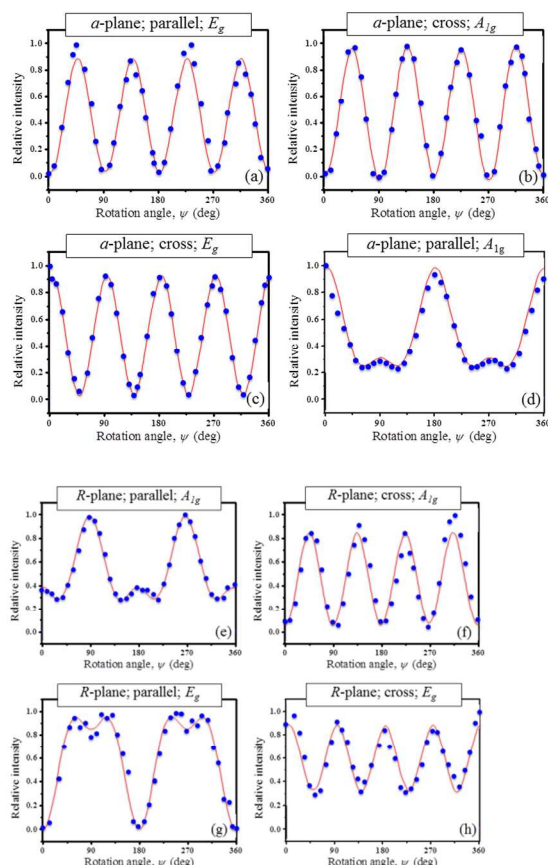


**Fig. 4:** Experimentally retrieved in-plane angular dependences of Raman intensity for different vibrational modes in both parallel and cross polarization configurations: (a)-(d) *a*-plane, (e)-(h) *R*-plane.

Table 3 compares the RTE values obtained from different crystallographic planes of sapphire, and shows their average values and statistical scatter. The quantitative knowledge of the full set of RTE constants represents the basis for the spectroscopic evaluation of local crystallographic orientation in polycrystalline alumina materials.

**Table 3** RTE values obtained from different crystallographic planes of sapphire (average values and statistical scatter).

Tensor elements	Mean square error	Polarization configuration	Polarization configuration
$a = -0.8$	$\pm 0.001$	Cross	<i>a</i> -plane <i>c</i> -axis
$b = 0.2$	$\pm 0.01$	Parallel	axis
$a = -0.8$	$\pm 0.014$	Cross	<i>m</i> -plane <i>c</i> -axis
$b = 0.2$	$\pm 0.001$	Parallel	axis

$a = -0.8$	$\pm 0.014$	Cross	<i>R</i> -plane <i>a</i> -axis
$b = 0.2$	$\pm 0.006$	Parallel	axis
$c = 0.015$	$\pm 0.07$	Cross	<i>a</i> -plane <i>c</i> -axis
$d = -0.49$	$\pm 0.008$	Parallel	axis
$c = 0.015$	$\pm 0.03$	Cross	<i>m</i> -plane <i>c</i> -axis
$d = -0.49$	$\pm 0.011$	Parallel	axis
$c = 0.015$	$\pm 0.02$	Cross	<i>R</i> -plane <i>a</i> -axis
$d = -0.49$	$\pm 0.01$	Parallel	axis

#### 4.2. Determination of PDP constants from 4-point uniaxial bending measurements.

The simplest approach to the calibration of PDP constants for a selected vibrational band consists in generating a known uniaxial stress field along a known direction of the investigated crystal. One way of doing so consists in loading a rectangular crystal bar in a four-point flexure jig. The jig, equipped with a load-cell, is then placed under the Raman microprobe, and Raman line scans are performed along its thickness to reveal the spectral shifts of selected bands as a function of the location along the bar thickness. Figure 5 shows a schematic draft of the bending calibration setup adopted in this study, including the uniaxial stress field, our choice of Euler angles, and the selected laboratory Cartesian system. The *x*-axis was set along the stress direction, while the *y*-axis was taken along the specimen thickness (i.e., along the loading direction) at the center of the bending bar. According to these choices, the uniaxial stress field can easily be expressed by a scalar quantity,  $\sigma_{ij} = \sigma_{xx}$ , with all the other tensor components being equal to zero. The calibration method using the four-point flexure configuration involves both compressive and tensile uniaxial stresses, whose maxima,  $\pm \sigma_{\max}$ , are of the same magnitude. The uniaxial stress field varies linearly along the bar thickness, as a function of the abscissa, *y*, as follows:

$$\sigma_{xx}(y) = \frac{2y}{h} \sigma_{\max} = \frac{2y}{h} \times \frac{3P(L-l)}{2wh^2} \quad (42)$$

where *P* is the (known) applied load, *w* and *h* are the width and the thickness of the bending bar, respectively, and *L* and *l* are the large and the small span of the bending jig, respectively (cf. Fig. 5).

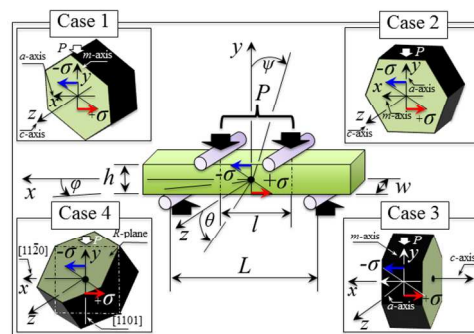


**Fig. 5:** Schematic draft of the bending calibration setup, including the uniaxial stress field, our choice of Euler angles, and the selected laboratory Cartesian system in 4 calibration configurations (Case 1-4) only differing in crystal orientation.

After having applied a given bending load, *P*, a series of Raman spectra can be collected at locations along the specimen

thickness, as a function of the abscissa,  $y$ . Since the uniaxial stress,  $\sigma_{xx}$ , is linked to the abscissa,  $y$ , through Eq. (42), the experimentally collected dependence,  $\Delta\omega(y)$ , can be promptly converted into the dependence,  $\Delta\omega(\pm\sigma_{xx})$ . In the simple case of uniaxial stress, Eqs. (25) and (35), for  $A_{1g}$  and  $E_g$  modes, respectively, can be greatly simplified and become:

$$\Delta\omega_A^{\perp\perp} = \Delta\omega_A = \frac{1}{2\omega_{0,A}} \left[ (K_1^A S_{11} + K_2^A S_{12} + K_3^A S_{13})(\cos\theta \cos\varphi \cos\psi - \sin\psi \sin\varphi)^2 \right. \\ \left. + (K_2^A S_{11} + K_1^A S_{12} + K_3^A S_{13})(\cos\psi \sin\varphi + \cos\theta \cos\varphi \sin\psi)^2 \right. \\ \left. + (K_1^A S_{13} + K_2^A S_{13} + K_3^A S_{33}) \sin^2\theta \cos^2\varphi \right] \sigma_{xx} \quad (43)$$

and

$$\Delta\bar{\omega}_E^{\perp\perp} = \frac{\sigma_{xx}}{2\omega_{0,E}} \left\{ [K_1^E (S_{11} + S_{12}) + K_2^E S_{13}] (\cos^2\theta \cos^2\varphi + \sin^2\varphi) + (2K_1^E S_{13} + K_2^E S_{33}) \sin^2\theta \cos^2\varphi \right. \\ \left. + \frac{I_{E_{g(x)}}^{\perp\perp} - I_{E_{g(y)}}^{\perp\perp}}{I_{E_{g(x)}}^{\perp\perp} + I_{E_{g(y)}}^{\perp\perp}} \times \left\{ [K_3^E (S_{11} - S_{12}) (\cos^2\theta \cos^2\varphi \cos 2\psi - \cos 2\psi \sin^2\varphi - \sin 2\varphi \cos\theta \sin 2\psi)] \right. \right. \\ \left. \left. + K_4^E [S_{44} (\cos\theta \sin\theta \cos^2\varphi \cos\psi - \sin\theta \cos\varphi \sin\psi \sin\psi)] \right. \right. \\ \left. \left. + 2S_{14} [(\sin^2\varphi - \cos^2\theta \cos^2\varphi) \sin\psi \cos\psi - \cos\theta \sin\varphi \cos\varphi \cos 2\psi] \right\}^2 \right. \\ \left. + \left\{ 2K_3^E [S_{14} (\cos\theta \sin\theta \cos^2\varphi \cos\psi - \sin\theta \cos\varphi \sin\psi \sin\psi)] \right. \right. \\ \left. \left. + (S_{11} - S_{12}) [(\sin^2\varphi - \cos^2\theta \cos^2\varphi) \sin\psi \cos\psi - \cos\theta \sin\varphi \cos\varphi \cos 2\psi] \right\} \right. \\ \left. + K_4^E [S_{14} (\cos^2\theta \cos^2\varphi \cos 2\psi - \cos 2\psi \sin^2\varphi - \sin 2\varphi \cos\theta \sin 2\psi)] \right. \\ \left. + S_{44} (-\cos\theta \sin\theta \cos^2\varphi \sin\psi - \sin\theta \cos\varphi \sin\psi \cos\psi) \right\}^{\frac{1}{2}} \quad (44)$$

Under the assumption of a linearly elastic deformation of the bending bar, the plot of spectral shifts,  $\Delta\omega(\sigma_{xx})$ , in the interval,  $-\sigma_{\max} \leq \sigma_{xx} \leq \sigma_{\max}$ , should be linear. The slope of such a plot depends on the vibrational mode analyzed and is related to a specific combination of PDP constants, as governed by Eqs. (43) and (44). It should be noted that, as far as the corundum structure is concerned, the full set of PDP constants includes 7 independent values, namely 3 and 4 constants for the  $A_{1g}$  and the  $E_g$  mode, respectively. In other words, one needs to carry out at least four uniaxial bending experiments along different crystallographic directions. According to the sample availability of both single-crystalline and polycrystalline nature in this study, we carried out five different bending calibration tests. In testing single-crystalline samples, the uniaxial stress field was applied in 4 different configurations, as follows: (Case 1) loading direction,  $m$ -axis; stress direction,  $a$ -axis ( $\theta = \varphi = \psi = 0$ ); (Case 2) loading direction,  $a$ -axis; stress direction,  $m$ -axis ( $\theta = \varphi = 0$ ;  $\psi = \frac{\pi}{2}$ ); (Case 3) loading direction,  $m$ -axis; stress direction,  $c$ -axis ( $\theta = \frac{\pi}{2}$ ;  $\varphi = \psi = 0$ ); and, (Case 4) loading along direction,  $[1101]$ ; stress direction,  $[11\bar{2}0]$  ( $\theta = \frac{29\pi}{90}$ ;  $\varphi = \frac{\pi}{6}$ ;  $\psi = \frac{\pi}{2}$ ). The four cases mentioned above are schematically depicted in Fig. 5 with reference to the orientation of the corundum structure. The equations derived from Eqs. (44) and (45), which are pertinent to the above 4 cases and give the predicted slopes of the plots  $\Delta\omega(\sigma_{xx})$ , can be listed, as follows:

Case 1:

$$\Delta\omega_A^{\perp\perp} = \frac{K_1^A S_{11} + K_2^A S_{12} + K_3^A S_{13}}{2\omega_{0,A}} \sigma_{xx} \quad (45)$$

$$\Delta\bar{\omega}_E^{\perp\perp} = \frac{\sigma_{xx}}{2\omega_{0,E}} \left\{ K_1^E (S_{11} + S_{12}) + K_2^E S_{13} + \frac{I_{E_{g(x)}}^{\perp\perp} - I_{E_{g(y)}}^{\perp\perp}}{I_{E_{g(x)}}^{\perp\perp} + I_{E_{g(y)}}^{\perp\perp}} \times \sqrt{[K_3^E (S_{11} - S_{12})]^2 + (K_4^E S_{14})^2} \right\} \quad (46)$$

Case 2:

$$\Delta\omega_A^{\perp\perp} = \frac{K_2^A S_{11} + K_1^A S_{12} + K_3^A S_{13}}{2\omega_{0,A}} \sigma_{xx} \quad (47)$$

$$\Delta\bar{\omega}_E^{\perp\perp} = \frac{\sigma_{xx}}{2\omega_{0,E}} \left\{ K_1^E (S_{11} + S_{12}) + K_2^E S_{13} + \frac{I_{E_{g(x)}}^{\perp\perp} - I_{E_{g(y)}}^{\perp\perp}}{I_{E_{g(x)}}^{\perp\perp} + I_{E_{g(y)}}^{\perp\perp}} \times \sqrt{[K_3^E (S_{11} - S_{12})]^2 + (K_4^E S_{14})^2} \right\} \quad (48)$$

Case 3:

$$\Delta\omega_A^{\perp\perp} = \frac{K_1^A S_{13} + K_2^A S_{13} + K_3^A S_{33}}{2\omega_{0,A}} \sigma_{xx} \quad (49)$$

$$\Delta\bar{\omega}_E^{\perp\perp} = \frac{\sigma_{xx}}{2\omega_{0,E}} (2K_1^E S_{13} + K_2^E S_{33}) \quad (50)$$

Case 4:

$$\Delta\omega_A^{\perp\perp} = \frac{\sigma_{xx}}{8\omega_{0,A}} \left[ (K_1^A S_{11} + K_2^A S_{12} + K_3^A S_{13}) + 3(K_1^A S_{12} + K_2^A S_{11} + K_3^A S_{13}) \cos^2 \frac{29\pi}{90} \right. \\ \left. + 3(K_1^A S_{13} + K_2^A S_{13} + K_3^A S_{33}) \sin^2 \frac{29\pi}{90} \right] \quad (51)$$

$$\Delta\bar{\omega}_E^{\perp\perp} = \frac{\sigma_{xx}}{8\omega_{0,E}} \left\{ [K_1^E (S_{11} + S_{12}) + K_2^E S_{13}] (3\cos^2 \frac{29\pi}{90} + 1) + 3(K_1^E S_{13} + K_2^E S_{33}) \sin^2 \frac{29\pi}{90} \right. \\ \left. + \frac{I_{E_{g(x)}}^{\perp\perp} - I_{E_{g(y)}}^{\perp\perp}}{I_{E_{g(x)}}^{\perp\perp} + I_{E_{g(y)}}^{\perp\perp}} \times \left\{ [K_3^E (S_{11} - S_{12}) (1 - 3\cos^2 \frac{29\pi}{90}) + \sqrt{3} K_4^E (2S_{14} \cos \frac{29\pi}{90} - S_{44} \sin \frac{29\pi}{90})]^2 \right. \right. \\ \left. \left. + \left\{ 2\sqrt{3} K_3^E [S_{14} \sin \frac{29\pi}{90} + (S_{11} - S_{12}) \cos \frac{29\pi}{90}] + K_4^E [S_{14} (1 - 3\cos^2 \frac{29\pi}{90}) - 3S_{44} \cos \frac{29\pi}{90} \sin \frac{29\pi}{90}] \right\}^2 \right\} \right\}^{\frac{1}{2}} \quad (52)$$

An additional bending experiment, henceforth referred to as Case 5, was carried out on a fine grained polycrystalline alumina sample with a random orientation of the grains. With the interaction between Raman probe and grain structure lying in the configuration depicted in Fig. 3(c), the expected slopes for the uniaxial calibration in a polycrystalline sample can be set as:

$$\Delta\omega_{A,p}^{\perp\perp} = \int_0^\pi \int_0^{2\pi} \int_0^{2\pi} \frac{\sin\theta}{8\pi} \Delta\omega_A d\theta d\varphi d\psi \\ = \frac{\sigma_{xx}}{6\omega_{0,A}} \left[ (S_{11} + S_{12} + S_{13}) (K_1^A + K_2^A) + (2S_{13} + S_{33}) K_3^A \right] \quad (53)$$

$$\Delta\omega_{E,p}^{\perp\perp} = \int_0^\pi \int_0^{2\pi} \int_0^{2\pi} \frac{\sin\theta}{8\pi^2} \Delta\omega_E d\theta d\varphi d\psi \\ = \frac{\sigma_{xx}}{6\omega_{0,E}} \left\{ 2 \left[ K_1^E (S_{11} + S_{12}) + K_2^E S_{13} \right] + (2K_1^E S_{13} + K_2^E S_{33}) \right. \\ \left. + 2 \frac{I_{E_{g(x)}}^{\perp\perp} - I_{E_{g(y)}}^{\perp\perp}}{I_{E_{g(x)}}^{\perp\perp} + I_{E_{g(y)}}^{\perp\perp}} \times \sqrt{[K_3^E (S_{11} - S_{12})]^2 + (K_4^E S_{14})^2} \right\} \quad (54)$$

where the subscript  $p$  refers to the polycrystalline nature of the sample. From solving the above set of Eqs. (45)-(54) at any location along the thickness of the sample loaded in bending geometry, values of the PDP constants for the available Raman bands can be retrieved.

According to the theoretical treatment given above, the PDP constants of the detected vibrational bands were extracted from five independent sets of calibration data in bending configuration, four sets collected on single-crystalline samples uniaxially loaded along different crystallographic directions, and one data set obtained from an untextured (fine-grained)  $Al_2O_3$  polycrystal. Figures 6(a)-(e) show bending calibration

plots of spectral shifts for the  $417\text{ cm}^{-1} A_{1g}$  vibrational mode as a function of uniaxial stress magnitude for the five different samples (Cases 1~5), in parallel polarization configuration. Linear fitting according to the least square method enabled us to retrieve the values of the slopes, as explicitly given in inset to Fig. 6.

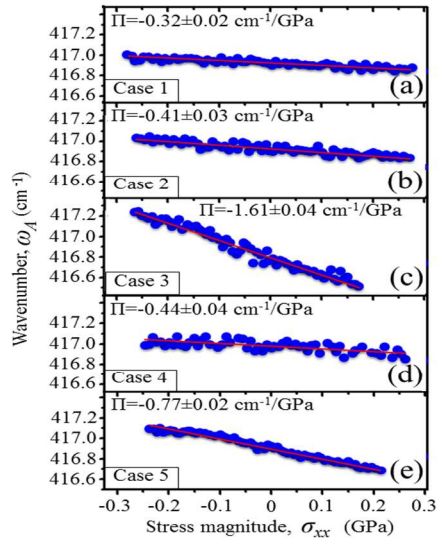


**Fig. 6:** Bending calibration plots of spectral shifts for the  $417\text{ cm}^{-1} A_{1g}$  vibrational mode as a function of uniaxial stress magnitude for five different samples (Cases 1~5). Data were collected in a parallel polarization configuration of the Raman probe. Linear fitting is shown for each plot according to the least square method.

Accordingly, a system of working equations could be obtained from Eqs. (45), (47), (49), and (51), as follows:

$$\begin{cases} K_1^A S_{11} + K_2^A S_{12} + K_3^A S_{13} = -267 \\ K_2^A S_{11} + K_1^A S_{12} + K_3^A S_{13} = -345 \\ K_1^A S_{13} + K_2^A S_{13} + K_3^A S_{33} = -1339 \\ (S_{11} + 3S_{12} \cos^2 \frac{29\pi}{90} + 3S_{13} \sin^2 \frac{29\pi}{90})K_1^A + (S_{12} + 3S_{11} \cos^2 \frac{29\pi}{90} + 3S_{13} \sin^2 \frac{29\pi}{90})K_2^A \\ + (S_{13} + S_{13} \cos^2 \frac{29\pi}{90} + 3S_{33} \sin^2 \frac{29\pi}{90})K_3^A = -1467 \\ (S_{11} + S_{12} + S_{13})(K_1^A + K_2^A) + (2S_{13} + S_{33})K_3^A = -1901 \end{cases} \quad (55)$$

All the obtained experimental plots were linear in the stress interval investigated, but exhibited different slopes. Similarly, for the  $378\text{ cm}^{-1} E_g$  mode, calibration plots obtained on the sapphire single-crystals and polycrystal are depicted in Figs. 7(a)-(e) (Cases 1~5). A system of independent equations could then be obtained, according to Eqs. (46), (48), (50), (52) and (54), as follows:

$$\begin{cases} K_1^E (S_{11} + S_{12}) + K_2^E S_{13} + \sqrt{[K_3^E (S_{11} - S_{12})]^2 + (K_4^E S_{14})^2} = -367 \\ 2K_1^E S_{13} + K_2^E S_{33} = -266 \\ [K_1^E (S_{11} + S_{12}) + K_2^E S_{13}] (3 \cos^2 \frac{29\pi}{90} + 1) + 3(2K_1^E S_{13} + K_2^E S_{33}) \sin^2 \frac{29\pi}{90} \\ - \frac{1}{2} \times \left\{ \left[ K_3^E (S_{11} - S_{12})(1 - 3 \cos^2 \frac{29\pi}{90}) + \sqrt{3} K_4^E (2S_{14} \cos \frac{29\pi}{90} - S_{44} \sin \frac{29\pi}{90}) \right]^2 \right. \\ \left. + \left\{ 2\sqrt{3} K_3^E \left[ S_{14} \sin \frac{29\pi}{90} + (S_{11} - S_{12}) \cos \frac{29\pi}{90} \right] \right\} \right\}^{\frac{1}{2}} = -1316 \\ + K_4^E \left[ S_{14} (1 - 3 \cos^2 \frac{29\pi}{90}) - 3S_{44} \cos \frac{29\pi}{90} \sin \frac{29\pi}{90} \right] \\ 2[K_1^E (S_{11} + S_{12}) + K_2^E S_{13}] + (2K_1^E S_{13} + K_2^E S_{33}) = -1021 \end{cases} \quad (56)$$

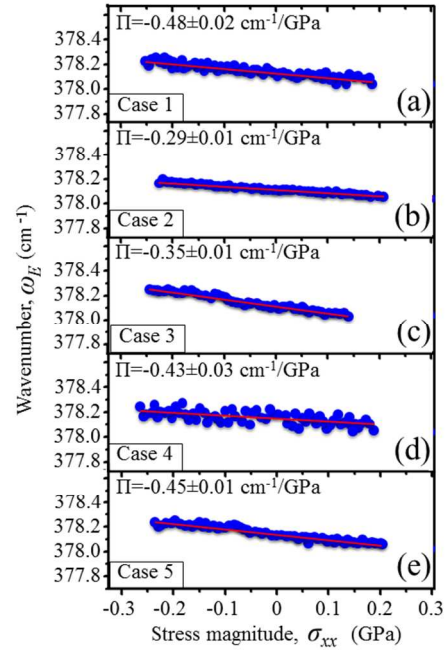


**Fig. 7:** Bending calibration plots of spectral shifts for the  $378\text{ cm}^{-1} E_g$  vibrational mode as a function of uniaxial stress magnitude for five different samples (Cases 1~5). Linear fitting is shown for each plot according to the least square method.

Upon solving the two independent systems of Eqs. (55) and (56), the two sets of PDP values,  $K_i^A$  ( $i=1,2,3$ ) and  $K_j^E$  ( $j=1,2,3,4$ ) could be determined, which corresponds to the  $417\text{ cm}^{-1}$  band of the  $A_{1g}$  mode and to the  $378\text{ cm}^{-1}$  band of the  $E_g$  mode, respectively. Similar procedures were also performed on the shifts recorded for the band located at around  $645\text{ cm}^{-1}$  (belonging to the  $A_{1g}$  vibrational mode), and for the three bands detected at around  $430$ ,  $578$ , and  $750\text{ cm}^{-1}$  (all belonging to the  $E_g$  vibrational mode). The values of PDP constants obtained for all the above-mentioned Raman bands are listed in Table 4. Note that one of the advantages of a uniaxial calibration in bending is that it is not affected by probe broadening along the sample depth. This characteristic is a direct consequence of the linear character of the stress distribution along the thickness of the bending bar, which is independent of sample depth.<sup>46</sup> In Table 4, the statistical scatter of the retrieved PDP constants is also shown, which helps to identify the degree of precision to which stress measurements can be made through exploiting the

sensitivity of each individual Raman band to a unitary stress state.

**Table 4** PDP constants obtained for all the observed Raman bands of the corundum structure of sapphire (average values and statistical scatter).

Band (cm <sup>-1</sup> )		$K_1$ (×10 <sup>3</sup> cm <sup>-2</sup> )	$K_2$ (×10 <sup>3</sup> cm <sup>-2</sup> )	$K_3$ (×10 <sup>3</sup> cm <sup>-2</sup> )	$K_4$ (×10 <sup>3</sup> cm <sup>-2</sup> )
378	$E_g$	-293±22	-227±24	-3.2±0.5	-8.5±1
417	$A_{1g}$	-396±19	-406±6	-777±18	--
430	$E_g$	-664±67	-613±74	-112±15	-30±5
576	$E_g$	-976±89	-721±76	-259±38	-16±3
645	$A_{1g}$	-610±69	-380±50	-764±73	--
750	$E_g$	-2117±319	-1193±166	-165±28	-35±4

### 4.3 Raman probe and local crystallographic assessments.

The key for understanding the angular dependence of the Raman intensities for the vibrational modes of sapphire resides in analyzing the change in the in-plane periodicity of the  $I_{E_g}^{\square}$  mode when the crystal plane varies from the  $a$ - to the  $c$ -plane. In terms of Euler angles, such a variation corresponds to an out-of-plane rotation by the angle,  $\theta$  (cf. Fig. 1(c)). Moving from

the  $c$ -plane ( $\theta = 0$ ) toward the  $a$ -plane ( $\theta = \frac{\pi}{2}$ ), the  $R$ -plane ( $\theta = \frac{58\pi}{180}$ ) corresponds to an intermediate configuration (cf. Fig. 1(c)). Figures 8(a) and (b) show the geometrical rotation of the crystal planes and the associated change in periodicity, respectively, with reporting the behavior of the Raman intensity,  $I_{E_g}^{\square}$ , upon rotation by the angle,  $\psi$ , in a single-crystal with crystallographic planes oriented at different angles,  $\theta$ . The algorithm reported in this study for the identification of the full set of three Euler angles for any arbitrary crystal orientation, based on the Raman selection rules, provides a set of independent Eqs. (8)-(14), which gives the general angular dependences of the Raman intensities of the  $A_{1g}$  and  $E_g$  phonon modes.

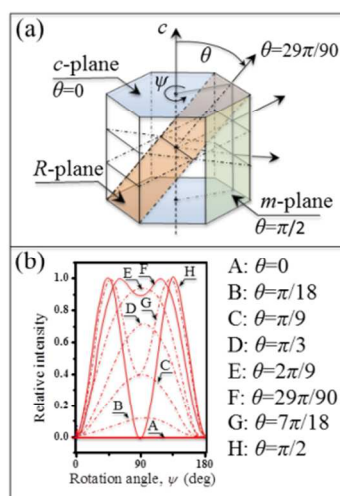


**Fig. 8:** (a) Schematic of the geometrical rotation of a crystal plane in the corundum structure by the Euler angle,  $\theta$ ; and, (b) the associated change in periodicity of the Raman intensity,  $I_{E_g}^{\square}$ , upon a rotation by the Euler angle,  $\psi$ , as a function of the angle,  $\theta$ .

With the knowledge of the 4 RTE elements for the sapphire structure (cf. Table 3), four independent working equations have become available for describing the polarized Raman intensities as a function of three unknown Euler angles. Any three of these four equations can be used to assess the three Euler angle needed for determining in space any unknown grain orientation. A viable experimental approach could consist in recording, at a fixed location on the surface of a polycrystalline sample, two series of parallel- and cross-polarized Raman spectra as a function of the in-plane rotation angle,  $\psi$ . Then, three angular dependencies can be selected among the four available ones (i.e.,  $I_{A_{1g}}^{\square}(\psi)$ ,  $I_{A_{1g}}^{\perp}(\psi)$ ,  $I_{E_g}^{\square}(\psi)$ , and  $I_{E_g}^{\perp}(\psi)$ ) and a best fitting routine run to determine the full set of Euler's angles. A computational algorithm was built up to automatically assess grain orientation from the collected spectra, and this procedure was applied to a polycrystalline alumina sample under different probe/microstructure interactions, as described in Figs. 3(a)-(c). Figures 9(a)-(f) summarizes the results of such crystallographic assessments under different conditions on the surface of polycrystalline  $Al_2O_3$ . In Figs. 9(a) and (b), rotation experiments and the fitting algorithm resolve the three Euler angles (given in the caption) for a single grain larger than the confocal Raman probe (cf. probe/microstructure interaction as shown in Fig. 3(a)), namely an abnormally grown grain found in the microstructural network. As the counterpart limit-case, Figs. 9(e) and (f) show a conspicuous absence of relative intensity dependence for both  $A_{1g}$  and  $E_g$  modes in the case of a large population of randomly oriented grains comprised in the Raman probe, as schematically shown in Fig. 3(c). In this latter case, the Raman measurement was conducted with a full aperture of the confocal pinhole, namely in a typically non-confocal configuration. Figures 9(c) and (d) show that it is still possible to detect in-plane angular dependences and, thus, to retrieve a set of (average) Euler angles in the case of only few grains comprised in the Raman probe, as in the case depicted in Fig. 3(b). When the Raman probe is applied in a confocal configuration (irradiation in the visible range and pinhole aperture of  $\sim 100 \mu m$ ), the case represented by Figs. 3(b) and 9(c)/(d) is actually the most commonly found one for polycrystalline  $Al_2O_3$  brands used in engineering applications (i.e., with an average grain size typically in the order of  $1 \mu m$ ). This point will be given a more detailed discussion in the next section. However, the important finding here is that the confocal Raman probe is still capable to provide us with an average crystal orientation (i.e., the one of the "probe mesocrystal") in polycrystalline  $Al_2O_3$ , through which we can run our tensor-resolved stress algorithm.

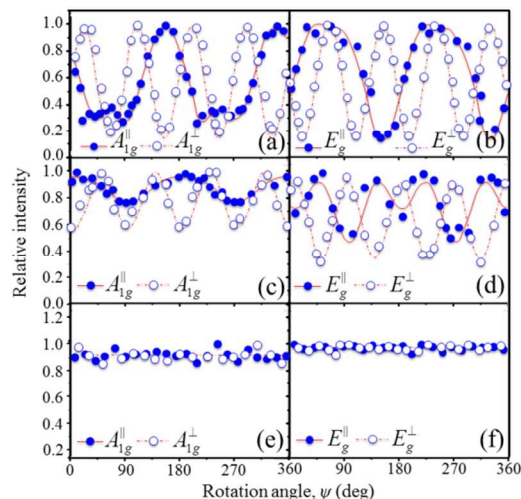


**Fig. 9:** (a)(b) Results of in-plane rotation experiments to resolve three Euler angles ( $\theta = \pi/4$ ;  $\varphi = 9\pi/25$ ;  $\psi = \pi/7$ ) for grain size larger than the confocal probe volume (cf. probe/microstructure interaction in Fig. 3(a)); (c)(d) in-plane angular dependences to resolve three (average) Euler angles ( $\theta = \pi/15$ ;  $\varphi = 13\pi/45$ ;  $\psi = \pi/9$ ) when only few grains are comprised in the Raman probe (cf. probe/microstructure interaction in Fig. 3(b)); and, (e)(f) in-plane angular rotation experiments show no periodical dependences for probe/microstructure interaction as depicted in Fig. 3(c).

#### 4.4 Data acquisition and computational protocols at the ceramic/metal interface.

As an application of the computational algorithms presented in the previous sections, we attempt hereafter the quantitative measurement of the complete set of tensor components for the case of a highly graded residual stress field stored into a polycrystalline alumina sample in the neighborhood of a metal joint. Figures 10(a) and (b) schematically show the overall geometry of the tested sample and the Raman measurement protocol, respectively. As discussed in previous sections of this paper, three different types of algorithm need to be merged together in order to achieve the desired outputs of stress analysis, namely the crystallographic algorithm based on Eqs. (8)-(14), the stress tensor computational algorithm based on Eqs. (25), (35) and (38), and the probe response algorithm based on Eqs. (39)-(41). The concurrent application of such algorithms requires the precise acquisition of various sets of Raman data in terms of both emission intensity and band shifts. As far as the analyses of crystallographic orientation and residual stress were concerned, a polarized Raman line-map was collected (in confocal configuration; pinhole aperture of  $100\ \mu\text{m}$ ) with the laser focused on the sample surface. The total length of the line scan was  $30\ \mu\text{m}$ , starting from the ceramic/metal interface (cf. abscissa,  $x$ , perpendicular to the ceramic/metal interface in Fig. 10(b)). A lateral step of  $0.5\ \mu\text{m}$  was maintained for the first  $12\ \mu\text{m}$  (i.e., where the stress gradient was expected to be steeper), while along the remaining length of the laser scan the lateral step was reduced to  $2\ \mu\text{m}$ . The local triplet of Euler angles at any given location could be retrieved from an in-plane rotation of  $\psi = 2\pi$  performed at the same location. However, due to an experimental difficulty in controlling the lateral sample displacement, rotation measurements were performed at locations every  $3\ \mu\text{m}$  away from the interface, within which same Euler angles were assumed. Raman peak shifts were recorded with respect to a reference peak position recorded under exactly the same

measurement conditions on an annealed (i.e., nominally stress-free) sapphire single-crystal sample.

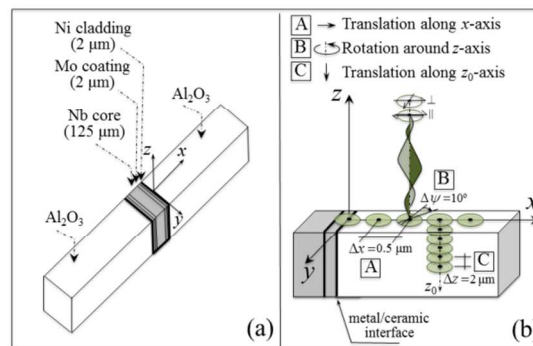


**Fig. 10:** (a) Geometry of the tested ceramic/metal joint sample, and (b) the Raman measurement protocol adopted for spatial and tensor resolved assessments of residual stress in the neighborhood of the interface.

Moreover, for investigating the stress gradient in the depth direction, by shifting the confocal probe at different depths,  $z$ , line-scan Raman measurements could be applied, with always keeping the lateral displacements set exactly along the same line of the surface scan. For comparison, band-shift profiles were also recorded (on the surface and at the same locations along the  $x$ -axis as those recorded for the Raman bands) for the fluorescence emission of the ruby lines of alumina. Regarding the assessment of PRF functions, both in-depth and in-plane Raman intensity scans were recorded and, based on those data, we determined the characteristic parameters  $p$ ,  $B$ , and  $\alpha_{\text{eff}}$  in Eq. (39). In-depth PRF measurements along the  $z$ -axis (cf. Fig. 10(b)) were performed with a step of  $2\ \mu\text{m}$  and repeated at each location of the line scan. For comparison, the PRF was also recorded at the same locations for the fluorescence emission of the ruby lines of alumina. From both Raman and fluorescence PRF data, an arbitrarily defined “probe depth”,  $z_d$ , was computed as the sample depth at which 90% of the overall band-intensity emission was contributed to the detected spectra. Figure 11 shows the recorded variations of Euler angles as a function of the abscissa,  $x$ , perpendicular to the ceramic/metal interface. The shown Euler angles refer to data collected at the surface of the sample and were obtained from Raman (relative) intensity data as a function of in-plane rotation angle,  $\psi$ , according to the same computational procedure shown in Sect. 4.3 and depicted in Fig. 10(b).

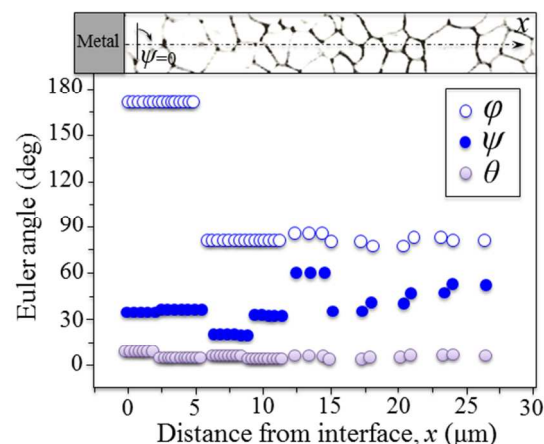


**Fig. 11:** Recorded variations of Euler angles at the sample surface as a function of an abscissa,  $x$ , perpendicular to the ceramic/metal interface ( $x=0$  corresponds to the location of the ceramic/metal interface). The microstructural arrangement at the measurement locations, as given in inset, was obtained from a filtered and sharpened cathodoluminescence image, which enabled us to visualize the grain boundaries on an otherwise featureless scanning electron micrograph of the polished surface.

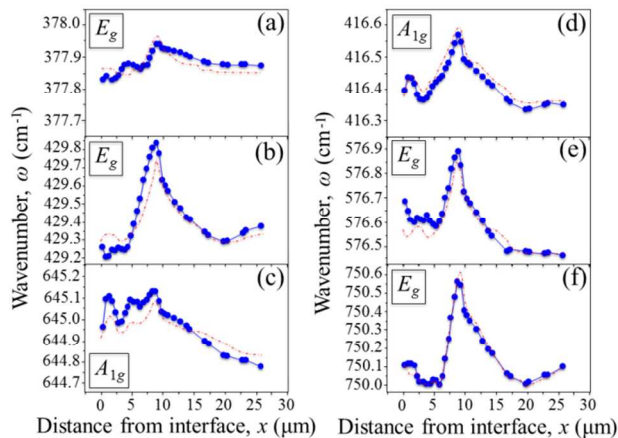


**Fig. 12:** Spectral band positions recorded on the free surface of the alumina polycrystal along a line scan across the interface; (a), (b), (c), (d), and (f) represent the variation in spectral position of Raman bands located at around 378, 429, 645, 418, 578, and 750  $\text{cm}^{-1}$ , respectively. The broken lines represent the results of the best-fitting routine applied according to Eq. (38) for resolving the stress tensor components as shown in the forthcoming Fig. 14.

Spectral band positions, as recorded on the free surface of the alumina polycrystal along the entire line scan, are shown in Fig. 12 for Raman bands located at around 417 and 645  $\text{cm}^{-1}$  (i.e., belonging to the  $A_{1g}$  vibrational mode), and 378, 430, 578, and 750  $\text{cm}^{-1}$  (i.e., belonging to the  $E_g$  mode).

In-depth PRF plots comparing Raman and fluorescence bands are shown in Figs. 13(a)-(d), as detected at increasing distances from the ceramic/metal interface. All the results retrieved for the characteristic parameters  $p$ ,  $B$ ,  $\alpha_{\text{eff}}$ , and  $z_d$  are listed in Table 5. Two striking features appear in the experimentally determined PRF functions, as displayed in Figs. 13(a)-(d) and Table 3: (i) the parameters  $p$ ,  $\alpha_{\text{eff}}$ , and  $z_d$  are functions of the distance from the metal interface; and, (ii) the Raman probe is found always conspicuously smaller than the fluorescence probe at each measurement location. The above circumstance (i) likely arises from a chemical gradient of metal ions diffused along the  $\text{Al}_2\text{O}_3$  grain boundaries during joining of the sample to the metallic component; the higher the concentration of metallic ions, the lower the penetration depth of the laser. From a computational point of view, the only consequence of this diffusional process is that the characteristic parameters  $p$ ,  $\alpha_{\text{eff}}$ , and  $z_d$  are functions of the abscissa,  $x$ , instead of being constants throughout the material. The latter circumstance (ii) is mainly a direct consequence of the absorption-re-emission of ruby line photons at  $\text{Cr}^{3+}$  sites, as already stated in the introductory section of this paper.

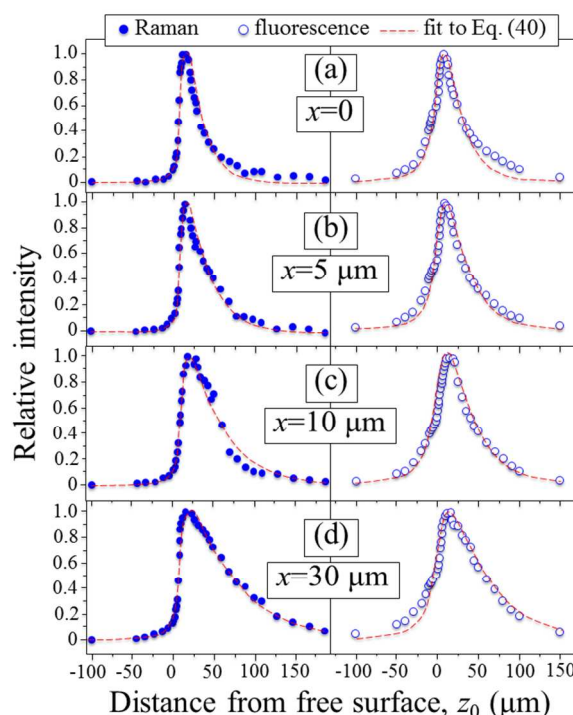


**Fig. 13:** In-depth PRF plots comparing the behavior of Raman and fluorescence bands as detected at increasing distances from the ceramic/metal interface; (a), (b), (c), and (d) for  $x=0$ , 5, 10, and 30  $\mu\text{m}$ , respectively.

**Table 5:** Characteristic parameters  $p$ ,  $B$ ,  $\alpha_{\text{eff}}$ , and  $z_d$  for the PRF of Raman and fluorescence emissions as a function of distance from the metal/ceramic interface.

	$x_0$ ( $\mu\text{m}$ )	$B$ ( $\mu\text{m}$ )	$p$ ( $\mu\text{m}$ )	$\alpha_{\text{eff}}$ ( $\mu\text{m}^{-1}$ )	$z_d$ ( $\mu\text{m}$ )
Fluorescence	Interface		10	0.030	16.1
	5		10	0.023	18.3
	10	$\sim 3.5$	13	0.020	22.4
	30		12	0.012	26.9
Raman	Interface		3.6	0.030	9.1
	5		3.2	0.037	7.8
	10	$\sim 2.0$	4.2	0.014	13.1
	30		5.1	0.010	16.7

With local Euler angles known from Eqs. (8)-(14), and the output of a computational routine based on Eq. (38) (i.e., as discussed in Sec. 2.3), we could obtain the profiles across the ceramic/metal interface for each individual stress component, as shown in Figs. 14(a)-(f) for the line scan performed with the confocal probe focused on the sample surface. A comparison between the experimental Raman band positions, as retrieved for each Raman band, and the convoluted curves representing the best-fitting solutions, which the algorithm of Eq. (38) has retrieved for stress-tensor deconvolution, are shown in Fig. 12. Discrepancies at any location are always  $<10\%$  and confirm the internal consistency of the adopted computational procedure.

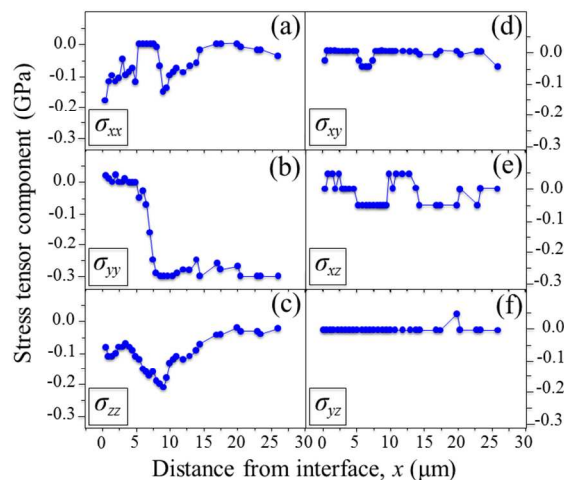


**Fig. 14:** Profiles across the ceramic/metal interface as retrieved for each individual stress tensor component on the line scan performed with the confocal probe focused on the sample free surface (i.e., the band-shift data in Fig. 12); tensor components  $\sigma_{xx}$ ,  $\sigma_{yy}$ ,  $\sigma_{zz}$ ,  $\sigma_{xy}$ ,  $\sigma_{xz}$ , and  $\sigma_{yz}$  in (a), (b), (c), and (d), respectively.

Repeating the same procedure for line-scans with the laser focus gradually shifted at several locations along the subsurface could also give one the possibility to perform a spatial deconvolution of the stress tensor profiles, according to the PRF algorithm expressed by the Eqs. (39)-(41). This approach takes advantage of the relatively high transparency of the material, and may contain more stress information than the method previously reported for surface stress analysis by using different probes, despite an equivalent trace of the principal stress tensor.<sup>47</sup> Figure 15 shows the deconvoluted profiles of the trace of the principal stress tensor,  $\langle \sigma_{ii}^* \rangle$ , as a function of depth,  $z$ , at different locations along the abscissa,  $x$ . This stress magnitude should play a fundamental role in the resistance of the joint to external loading. The retrieved stress profiles could always be fitted to an equation of the type:<sup>48-50</sup>

$$\langle \sigma_{ii}^* \rangle(z) = n_1 \frac{n_2 + n_3(z - n_4)}{n_2^2 + (z - n_4)^2} \quad (57)$$

with the values of the constants  $n_1$ ,  $n_2$ ,  $n_3$ , and  $n_4$  depending on the location of the measurement and thus function of the Cartesian coordinate,  $x$  (cf. values listed in Table 6). The residual stress magnitude on the sample surface was always strongly compressive with higher values in the very neighborhood of the interface, as dictated by the lower thermal expansion coefficient of  $\text{Al}_2\text{O}_3$  as compared to the metal phases. However, upon proceeding along the sample depth, a steep stress gradient could be found with a maximum of (weak) tensile stress along the subsurface until reaching a stress free state (cf. Fig. 15). It should also be noted that the dependence of the function,  $\langle \sigma_{ii}^* \rangle(z)$ , on probe location was not only a consequence of the stress gradient along the  $x$ -axis (i.e., as it should be expected due to the presence of the ceramic/metal interface), but also of the local stresses associated with the size and local orientation of the  $\text{Al}_2\text{O}_3$  grains. In this context, therefore, the confocal Raman probe proved capable to capture such second-order effect in the local three-dimensional stress distribution.

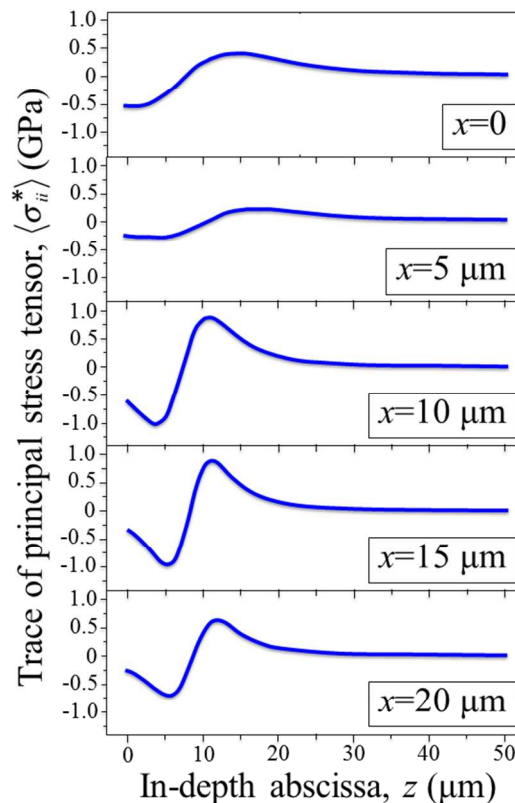


**Fig. 15:** Deconvoluted profiles of the trace of the principal stress tensor,  $\langle \sigma_{ii}^* \rangle$ , as a function of depth,  $z$ , at different locations along the abscissa,  $x$ . All plots were found to obey Eq. (57) with the values of the constants  $n_1$ ,  $n_2$ ,  $n_3$ , and  $n_4$  listed in Table 6.

**Table 6:** Values of the constants  $n_1$ ,  $n_2$ ,  $n_3$ , and  $n_4$  as displayed in Eq. (57), which describes the in-depth stress profiles as a function of the location of the measurement across the metal/ceramic interface.

	$x=0$ $\mu\text{m}$	$x=5$ $\mu\text{m}$	$x=10$ $\mu\text{m}$	$x=15$ $\mu\text{m}$	$x=20$ $\mu\text{m}$	$x=25$ $\mu\text{m}$
$n_1$	72869	61750	14839	14878	16403	11146
$n_2$	-10.5	-10.2	-5.0	-5.2	-5.5	-3.3
$n_3$	25	15	18	23	20	19
$n_4$	7	10	7	8	8.5	6

#### 4.5 Validation of the stress algorithm in comparison with fluorescence spectroscopy.

In the context of this paper, a comparison between fluorescence and Raman data in terms of residual stress profiles is considered a central task for validating the newly proposed algorithm for tensorial and spatial deconvolutions of stress fields in polycrystalline alumina. However, a direct comparison between the spectroscopic outputs of the two probes is definitely not a straightforward task. There are mainly two fundamental differences, inherent to the different physical nature of the two probes, which have to be taken into consideration: (i) the fluorescence probe experiences a spectral shift that is proportional to the trace of the principal stress

tensor,  $\langle \sigma_{ii}^* \rangle$ , namely, to the algebraic sum of the three hydrostatic components of the stress tensor when represented in a selected Cartesian frame that diagonalizes it (i.e.,  $\sigma_{ij} = 0$  for  $i \neq j$ ),<sup>51</sup> and, (ii) the parameters of the PRF are substantially different for the two probes (cf. Table 5), and thus there exist a conspicuous difference in spatial resolution between Raman and fluorescence measurements. This latter circumstance plays a role when highly graded stress fields, as in the case of metal/ceramic interfaces, are probed. In order to match these differences in spectroscopic characteristics, we first diagonalized the stress tensor components in Fig. 12 (i.e., those obtained from Raman data) at each location along the line-scan profile and then computed the related tensor trace,  $\langle \sigma_{ii}^* \rangle$ , from the diagonalized tensors as a function of the abscissa,  $x$ . As an additional procedure to make comparable the depth resolution of the two probes, we exploited the knowledge of the function,  $\langle \sigma_{ii}^* \rangle(z)$ , at each location (cf. Eq. (57) and Fig. 15) to normalize the two probes to the same depth,  $z_0$ , through their respective PRF parameters. Figure 16 shows a comparison between the outputs of the two probes in terms of trace of the stress tensor,  $\langle \sigma_{ii}^* \rangle$ . The shift of the fluorescence  $R_1$  line was converted into the stress magnitude,  $\langle \sigma_{ii}^* \rangle$ , by means of the piezo-spectroscopic tensor given by He and Clarke.<sup>7</sup> The reasonable agreement observed between the two sets of data proves the consistency between the responses of the two different probes. It also becomes clear that, unlike fluorescence, the Raman spectrum possesses inherent information of the stress tensor components, while being also capable to resolve local fluctuations of stresses related to the polycrystalline nature of the sample.

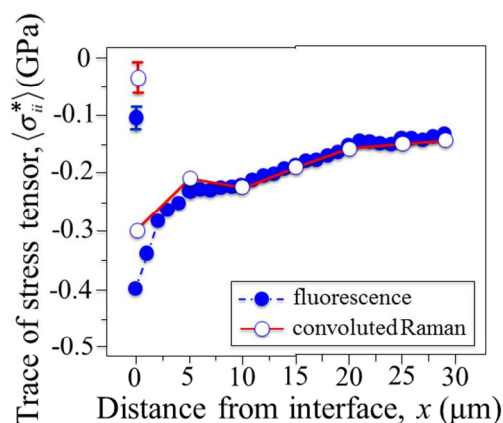


**Fig. 16:** Comparison between the outputs of the Raman and fluorescence probes for data collected at exactly the same locations in terms of trace of the stress tensor,  $\langle \sigma_{ii}^* \rangle$ . The comparison proves the consistency between the responses of the two different probes, thus validating our newly proposed Raman protocol for stress tensor assessments. Related error bars were also provided in the figure.

#### 4.6 Importance of the present findings in the applicative world

While Raman spectroscopy is nowadays an established and powerful tool in non-invasive real-time analysis and diagnostics for a wide range of samples, its translation into practical

applications is yet, in the majority of the cases, impeded by an intrinsic lack of robustness of the related spectroscopic algorithms and calibration models. This paper indeed proves that Raman algorithms might become quite complicated and cumbersome when applied to polycrystalline matter, and this has been the main reason for their applicative delay. However, with advanced applications progressing day by day towards new frontiers of science, systematic approaches are yet missing that could fully expand the Raman method to the real industrial world. Such approaches can only start from basic concepts of group theory, but they have to reach a more practical state, in which expanded and workable algorithms of selection rules and secular equations could actually be employed in industrial research and development. This paper has solved for the first time the experimental problem of tensorial deconvolution of three-dimensional microscopic stress states in polycrystalline matter for trigonal crystals. The general user through computer routines can easily automatize the equations, now established and validated, in order to become user friendly at their final stage. In this development, our main driving force has been the strong request from the industrial world for a fully non-destructive approach (yet missing) to quantitatively extract, at a microscopic scale, shear stress components from the Raman spectrum, and to apply this practice to non-destructive stress analyses and quality control. We had in mind not only ceramic/metal joints, as explicitly shown in this paper, but also the bearing surfaces of artificial hip and knee joints in the field of joint arthroplasty (in which alumina is largely employed)<sup>52</sup> and alumina coating applications used in various structural and electronic fields.<sup>53</sup> Our findings here thus solve a long-standing problem in material physics through a physical chemistry approach, and pave the way to systematic (and non-destructive) reliability assessments of component quality from the micromechanical viewpoint. An arguable criticism to our expanded approach could be that the solution presented in this paper actually fills the gap between the formalism and the true materials only in a pragmatic way. The devil is in the scale (or gradients) of the local stress fields built up at grain boundaries. The concept of “mesocrystalline” Raman probe can actually be equated to that of the “mesh unit” in finite element analyses, the finer the mesh the more accurate the computation. From this point of view, our Raman approach has translated a problem of solid-state physics into an engineering problem, although any further improvement in spatial resolution of the stress analysis must await a technological breakthrough in efficiency of the Raman hardware.

## 5 Conclusions

A spectroscopic method has been proposed to extract the full set of stress tensor components from polarized Raman measurements. Theoretical formulations were first worked out to establish the dependences on both crystallographic orientation and stress state of the  $A_{1g}$  and  $E_g$  Raman modes of sapphire with corundum structure. Then, RTE and PDP constants for both  $A_{1g}$  and  $E_g$  modes were experimentally determined by means of a series of controlled experiments on differently oriented single-crystalline sapphire samples and a polycrystalline  $\text{Al}_2\text{O}_3$  sample. With the quantitative knowledge of these two sets of physical constants, the tensorial determination of unknown stress fields has become a generally feasible task. Accordingly, a reliable analytical tool has become available, which builds upon the already known versatility of Raman spectroscopy in materials analyses. A computer-aided procedure has also been suggested for removing averaging

effects that arise from the finite size of the optical probe and restoring spatial resolution. An experimental confirmation of the overall working algorithm (i.e., including crystallographic, stress-tensorial and spatial probe deconvolutions) could be obtained by measuring the highly graded residual stress field stored at a bonded interface between polycrystalline alumina and a layer of Nb/Mo/Ni metal. Measurements at exactly the same locations across the interface were performed with collecting both Raman and fluorescence emissions, namely two physically independent spectroscopic tools. After taking into account the different nature of the two probes, the stress results showed good agreement, thus validating the newly developed Raman algorithm by means of the more conventional fluorescence method. Although both experimental and computational procedures for tensor-resolved stress analyses in polycrystalline samples are lengthy when manually applied, they could be easily implemented into an automatic computer routine and eventually become adopted in routine industrial practices. The procedure shown in this paper could be extended to other polycrystalline samples with non-cubic structure and, thus, opens the way to fully tensor-resolved analyses of stress fields in polycrystalline ceramics, a long missing item in the otherwise flourishing panorama of Raman spectroscopy.

## Notes and references

<sup>a</sup> Ceramic Physics Laboratory, Kyoto Institute of Technology, Sakyo-ku, Matsugasaki, 606-8585, Kyoto, Japan.

\* Corresponding author; e-mail: pezzotti@kit.ac.jp

- 1 Q. Ma and D. R. Clarke, *J. Am. Ceram. Soc.*, 1994, **77**, 298.
- 2 Q. Ma and D. R. Clarke, *J. Am. Ceram. Soc.*, 1995, **78**, 1433.
- 3 U. J. Gibson and M. Chernuschenko, *Optics Express*, 1999, **4**, 443.
- 4 H. Mahiou, A. Beakou, and R. J. Young, *J. Mater. Sci.*, 1999, **34**, 6069.
- 5 L. Grabner, *J. Appl. Phys.*, 1978, **49**, 580.
- 6 R. A. Forman, G. J. Piermarini, J. D. Barnett, and S. Block, *Science*, 1972, **176**, 284.
- 7 J. He and D. R. Clarke, *J. Am. Ceram. Soc.*, 1995, **78**, 1347.
- 8 J. He and D. R. Clarke, *J. Am. Ceram. Soc.* 1997, **80**, 69.
- 9 M. Chai and J. M. Brown, *Geophys. Res. Lett.*, 1996, **23**, 3539.
- 10 D. J. Gardiner, M. Bowden, S. H. Margueron, and D. R. Clarke, *Acta Mater.*, 2007, **55**, 3431.
- 11 M. R. Gallas, Y. C. Chu, and G. J. Piermarini, *J. Mater. Res.*, 1995, **10**, 2817.
- 12 W. Jia and W. M. Yen, *J. Raman Spectrosc.*, 1989, **20**, 785.
- 13 G. H. Watson Jr., W. B. Daniels, and C. S. Wang, *J. Appl. Phys.*, 1981, **52**, 956.
- 14 M. Mariee and J. P. Mathieu, *C.R. Acad. Sci.*, 1946, **223**, 147.
- 15 E. Anastassakis, A. Pinczuk, E. Burstein, F. H. Pollak, and M. Cardona, *Sol. Stat. Commun.*, 1970, **8**, 133.
- 16 F. Cerdeira, C. J. Buchenauer, F. H. Pollak, and M. Cardona, *Phys. Rev. B*, 1972, **5**, 580.
- 17 V. J. Tekippe, A. K. Ramdas, and S. Rodriguez, *Phys. Rev. B*, 1973, **8**, 706.
- 18 V. Darakchieva, T. Paskova, M. Schubert, H. Arwin, P. P. Paskov, B. Monemar, D. Hommel, M. Heuken, J. Off, F. Schplz, B. A. Haskell, P. T. Fini, J. S. Speck, and S. Nakamura, *Phys. Rev. B*, 2007, **75**, 195217.
- 19 R. J. Briggs and A. K. Ramdas, *Phys. Rev. B*, 1976, **13**, 5518.
- 20 G. Pezzotti, *J. Appl. Phys.*, 2013, **113**, 211301.
- 21 G. Pezzotti, K. Okai, and W. Zhu, *J. Appl. Phys.*, 2012, **111**, 013504.
- 22 G. Pezzotti, H. Hagihara, and W. Zhu, *J. Phys. D: Appl. Phys.*, 2013, **46**, 145103.
- 23 W. Zhu, A. Leto, K. Hashimoto, and G. Pezzotti, *J. Appl. Phys.*, 2012, **112**, 103256.
- 24 W. Zhu and G. Pezzotti, *J. Raman Spectrosc.*, 2011, **42**, 2015.
- 25 W. Zhu and G. Pezzotti, *J. Appl. Phys.*, 2011, **109**, 073502.
- 26 S. Ohtsuka, W. Zhu, S. Tochino, Y. Sekiguchi, and G. Pezzotti, *Acta Mater.*, 2007, **55**, 1129.
- 27 W. L. Zhu, M. C. Munisso, A. Matsutani, W. Y. Ge, and G. Pezzotti, *Appl. Spectrosc.*, 2009, **63**, 185.
- 28 K. S. Wan, S. Tochino, S. Ohtsuka, W. L. Zhu, and G. Pezzotti, *J. Phys. D: Appl. Phys.*, 2010, **43**, 205501.
- 29 A. G. Evans, *Acta Metall.*, 1978, **26**, 1845.
- 30 R. C. Powell and B. Dibartolo, *Phys. Stat. Sol. (a)*, 1972, **10**, 315.
- 31 S. Rhagarantan and T. Venkatarayuda, *Proc. Indian. Acad. Sci.*, 1939, **29A**, 224.
- 32 S. P. S. Porto and R. S. Krishnan, *J. Chem. Phys.*, 1967, **47**, 1009.
- 33 G. H. Watson Jr. and W. B. Daniels, *J. Appl. Phys.*, 1981, **52**, 956.
- 34 R. S. Krishnan, *Proc. Indian. Acad. Sci.*, 1947, **26A**, 450.
- 35 H. W. Kunert, A. G. J. Machatine, A. Hoffmann, G. Kaczmarczyk, U. Haboock, J. Malherbe, J. Barnas, M. R. Wagner, and J. D. Brink, *Mater. Sci. Eng.*, 2007, **27**, 1222.
- 36 R. Loudon, *Adv. Phys.*, 1964, **13**, 423.
- 37 T. Goto, O. L. Anderson, I. Ohno, and S. Yamamoto, *J. Geophys. Res.*, 1989, **94**, 7588.
- 38 S. Narayanan and S. R. Kalidindi, *J. Appl. Phys.*, 1997, **82**, 2595.
- 39 H. S. Peiser, J. B. Wachtman, Jr., and R. W. Dickson, *J. Res. Natl. Bur. Stand. (US) A*, 1963, **67**, 395.
- 40 S. Venugopalan and A. K. Ramdas, *Phys. Rev. B*, 1973, **8**, 717.
- 41 A. Atkinson, S. C. Jain, and S. J. Webb, *Semicond. Sci. Technol.*, 1999, **14**, 561.
- 42 D. M. Lipkin and D. R. Clarke, *J. Appl. Phys.*, 1995, **77**, 1855.
- 43 W. L. Zhu and G. Pezzotti, *Appl. Spectrosc.*, 2005, **59**, 1042.
- 44 MATHEMATICA 7.0, Wolfram Research, Inc. (Champaign, IL, USA).
- 45 K. Okai, W. Zhu, and G. Pezzotti, *Phys. Stat. Sol. (a)*, 2011, **208**, 1132.
- 46 G. Pezzotti, W. Zhu, A. Leto, A. Matsutani, and A. A. Porporati, *J. Phys. D: Appl. Phys.*, 2006, **39**, 4975.
- 47 G. Pezzotti, Y. Takahashi, W. Zhu, and N. Sugano, *Wear*, 2012, **284-285**, 91.
- 48 F. Grellner, S. Hoescheler, P. Greil, J. Sindel, and A. Petschelt, *J. Mater. Sci.*, 1997, **32**, 6235.
- 49 R. G. Sparks and M. A. Paesler, *J. Appl. Phys.*, 1992, **71**, 891.
- 50 B. Eigenmann and E. Macherlauch, *Mat-wiss. u. Werkstofftech.*, 1995, **26**, 148.
- 51 E. Bonera, M. Fanciulli, and D. N. Batchelder, *J. Appl. Phys.*, 2003, **94**, 2729.
- 52 G. Pezzotti, *Advanced materials for joint implants* (Pan Stanford, Singapore, 2013), Chapters 3-5.
- 53 H. Herman and S. Sampath, *Thermal spray coatings, in Metallurgy and Ceramic Protective Coatings*, Edited by K. H. Stern (Chapman & Hall, London, UK, 1996), pp. 161-289.